

This item is the archived peer-reviewed author-version of:

Development of a ligand for in vivo imaging of mutant huntingtin in Huntington's disease

Reference:

Bertoglio Daniele, Bard Jonathan, Hessmann Manuela, Liu Longbin, Gärtner Annette, De Lombaerde Stef, Huscher Britta, Zajicek Franziska, Miranda Menchaca Alan, Peters Finn,- Development of a ligand for in vivo imaging of mutant huntingtin in Huntington's disease
Science translational medicine - ISSN 1946-6234 - 14:630(2022), eabm3682
Full text (Publisher's DOI): <https://doi.org/10.1126/SCITRANSLMED.ABM3682>
To cite this reference: <https://hdl.handle.net/10067/1865850151162165141>

28 **One Sentence Summary:** A small molecule that quantifies the causative agent of Huntington's
29 disease can be used to assess the efficacy of therapeutic interventions

30

31 **Abstract**

32 Huntington's disease (HD) is a dominantly inherited neurodegenerative disorder caused by a CAG
33 trinucleotide expansion in the huntingtin (*HTT*) gene that encodes the pathologic mutant HTT
34 (mHTT) protein with an expanded polyglutamine (PolyQ) tract. Whereas several therapeutic
35 programs targeting mHTT expression have advanced to clinical evaluation, methods to visualize
36 mHTT protein species in the living brain are lacking. Here we demonstrate the development and
37 characterization of a positron emission tomography (PET) imaging radioligand with high affinity
38 and selectivity for mHTT aggregates. This small molecule radiolabeled with ^{11}C ($[^{11}\text{C}]\text{CHDI-}$
39 180R) allowed non-invasive monitoring of mHTT pathology in the brain and could track region-
40 and time-dependent suppression of mHTT in response to therapeutic interventions targeting mHTT
41 expression in a rodent model. We further showed that in these animals, therapeutic agents that
42 lowered mHTT in the striatum had a functional restorative effect that could be measured by
43 preservation of striatal imaging markers, enabling a translational path to assess the functional
44 effect of mHTT lowering.

45

46 INTRODUCTION

47 Neurodegenerative disease pathology is characterized by the presence of insoluble protein deposits
48 in different subcellular compartments, which mark alterations in cellular homeostasis. Typically,
49 neurodegenerative disorders have a complex molecular etiology, and affected brain cells display
50 aggregation of a variety of proteins. In Huntington's disease (HD), a CAG-tract expansion beyond
51 39 repeats in exon-1 of the huntingtin (*HTT*) gene is sufficient to cause the disease in a fully
52 penetrant manner (1). HD can be considered a multi-system atrophy disorder, even though the
53 main pathological findings show ample degeneration of spiny projection neurons (SPNs) in the
54 caudate and putamen, neurons in the globus pallidus and subthalamic nucleus of the basal ganglia,
55 as well as substantial but variable degeneration in neurons of the cerebral cortex and thalamic,
56 cerebellar and hypothalamic nuclei (2). Mutant huntingtin (mHTT) protein deposition in the
57 neuropil and nucleus has variable morphology, is more frequent in some classes of projection
58 neurons than in interneurons, and less frequent in cells of glial origin. A well-described progression
59 "map" of degeneration pathology and aggregate deposition has been available for some time,
60 although it is not clear how well histopathological changes inform the clinical staging of HD (2,
61 3).

62 A longstanding goal for HD has been to target the cause of the disease. Therapeutic programs
63 targeting HTT expression have advanced to clinical stages, including a now-terminated open-label
64 extension study and Phase 3 trial that were evaluating the sustained safety and efficacy of
65 tominersen, an antisense oligonucleotide (ASO) delivered intrathecally that can lower both mutant
66 and wildtype (wt) HTT (4, 5) (www.clinicaltrials.gov, identifier NCT03842969, NCT03761849,
67 NCT03342053). The first gene therapy vector-mediated Phase 1/2 trial is now underway testing
68 AMT-130, an adeno-associated virus (AAV) AAV5-miRNA targeting both *HTT* alleles delivered
69 directly into the caudate and putamen of HD patients (6) (www.clinicaltrials.gov, identifier
70 NCT04120493). Delivery of both of these agents is invasive and characterized by a restricted
71 distribution that varies due to the modalities employed: the ASO predominantly decreases HTT
72 expression in the spinal cord, cortical areas, and cerebellum, with some drugs reaching deeper
73 basal ganglia nuclei, whereas the AAV-miRNA targets mostly the striatum and associated
74 connected cell bodies via axonal transport (6, 7). Although the distribution and pharmacological
75 activity of these therapeutics have been extensively evaluated in nonhuman primates and mHTT-

76 expressing transgenic minipigs (7) it is unclear whether we can expect a similar distribution in the
77 larger human brain.

78 A key milestone was reached when the Ionis/Roche Phase 1/2a trial (4) (www.clinicaltrials.gov,
79 identifier NCT02519036) showed for the first time sustained dose- and time-dependent decreases
80 in cerebrospinal fluid (CSF) concentration of mHTT, demonstrating pharmacological activity in
81 the human CNS. Regrettably, this finding has not led to clinical benefit in the recently terminated
82 Phase 3 tominersen trial, and analyses are underway to understand the safety issues identified,
83 which led to a worsening of disease symptoms in the cohort treated once every 8 weeks. How the
84 reduction of mHTT in CSF after delivery of ASOs via lumbar puncture and AAVs delivered into
85 brain parenchyma (5, 7) relates to lowering in affected circuits in the brain remains unclear.

86 To evaluate regional pharmacological effects of candidate therapeutics targeting mHTT, we sought
87 to develop a non-invasive imaging agent specific for aggregated mHTT that could give insight into
88 the timing, durability, and regional therapeutic effects of administered drugs (8-10). As all current
89 therapeutic agents in development (11) target either *HTT* or HTT transcriptional or post-
90 transcriptional processes, quantification of mHTT protein could offer a good indicator of the extent
91 of HTT lowering and of the biodistribution of the agents. [¹¹C]CHDI-180R was identified and
92 developed into a PET tracer through a medicinal chemistry campaign from an initial small
93 molecule screen that yielded mutant HTT aggregate binders (8-10). CHDI-180 is a high-affinity
94 (1-3 nM), cell-permeable ligand, specific for mHTT aggregates and unable to bind unexpanded
95 HTT, monomeric soluble mHTT, or nuclear inclusion bodies. We have demonstrated binding to
96 mHTT-derived fibrils generated from recombinant protein, and mHTT-aggregates expressed in
97 mouse HD models and human HD samples, whose precise state(s) (for example oligomer or
98 protofibril) have yet to be defined.

99 Here, we investigate the utility of a PET imaging ligand with high affinity and selectivity for
100 mHTT aggregation to detect mHTT aggregation in affected brain cells and its application as
101 indicator of pharmacological activity of agents that target HTT expression in the living brain.
102 Specifically, we describe the ability of [¹¹C]CHDI-180R, to identify time-, dose- and region-
103 specific pharmacological effects in two distinct interventional paradigms: direct striatal delivery
104 of AAVs expressing zinc finger protein (ZFP) repressors selectively targeting mHTT (12) in the
105 zQ175 HD mouse model (13, 14), and in a genetically regulatable Q140 knock-in HD mouse

106 model, the LacQ140^L(*), that enables ~50% systemic lowering of *mHtt* mRNA and mHTT protein
107 in a time-controlled manner. We further explore whether imaging agents for striatal markers with
108 diminished expression in HD (specifically phosphodiesterase 10a, PDE10a, and dopamine
109 receptors) (8, 15-19) can detect the protective effects of mHTT lowering interventions in a time-
110 dependent manner and serve as functional response indicator for mHTT lowering with
111 translational potential.

112

113 **RESULTS**

114 **CHDI-180 specifically binds mHTT in HD animal models**

115 Aggregate pathology was detected with [³H]CHDI-180 autoradiography (ARG) already at 4 weeks
116 of age in R6/2 mice (Fig. 1A,B). In the zQ175DN heterozygous (het) model, aggregation is slower
117 but detectable binding was measured at 6 months of age, increasing progressively until 13 months
118 of age (Fig. 1C,D), in a pattern that mirrors histological analysis using mEM48 detection (20).
119 Since R6/2 and the zQ175DN models express large expansions in the polyQ tract, we explored the
120 HdhQ80 knock-in (KI) model (21) expressing smaller CAG lengths to understand if aggregate
121 pathology could be detected with finer temporal and spatial manner. Fig. 1E,F shows that CHDI-
122 180 binding follows a ventro-dorsal gradient of aggregation within the striatum of HdhQ80
123 animals, beginning at 12 months of age in the homozygotes (hom). This pattern of aggregate
124 pathology within the striatum was confirmed histochemically (Fig. 1G,H) with mEM48 antibody
125 detection.

126

127 **CHDI-180 does not colocalize with nuclear inclusion bodies in HD animal models and** 128 **human brains**

129 The CHDI-180 ligand was initially identified using radioligand binding assays for expanded HTT
130 proteins produced recombinantly (8). However, mHTT aggregates can have different forms and
131 can be detected in distinct subcellular compartments (intranuclear inclusions, diffuse nuclear-
132 aggregated species, soma-localized aggregates, or neuropil aggregates). These species of
133 oligomerized/aggregated mHTT can be detected with antibodies against aggregated, polyQ
134 expanded mHTT, such as mEM48 (22) or PHP-1 (23). Therefore, we conducted double co-

135 detection studies (binding and immunostaining), using [³H]CHDI-180 ARG and mEM48
136 immunohistochemistry (IHC) (Fig. 1I-J; Fig. S1 and S2) in brain sections derived from zQ175DN
137 and HdhQ80 mice and post-mortem human HD carriers. CHDI-180 binding did not co-localize
138 with intranuclear inclusions detected by mEM48 in the zQ175DN model (Fig. 1I; Fig. S2A-S2C)
139 or in the HdhQ80 mouse model (Fig. 1J; Fig. S1), with most signal observed outside the nucleus,
140 presumably to neuropil or soma-localized mHTT aggregates. A similar pattern is observed in
141 human brain samples from HD individuals (Fig. 1K; Fig. S2G). There was no binding to the wt
142 mouse brain (Fig. S1J-S1L, S2D-S2F) nor in the brains of unaffected human subjects (Fig. S2H)
143 either in the grey or white matter under the autoradiographic conditions employed.

144

145 **[¹¹C]CHDI-180R PET imaging enables in vivo quantification of mHTT pathology**

146 To examine the in vivo kinetic properties of [¹¹C]CHDI-180R (8) as a PET ligand, we selected the
147 zQ175DN model because it displays a moderately slow disease onset with hallmark of mHTT-
148 aggregates increasing from 3 to 12 months (20). We performed in vivo microPET studies in 9-
149 month-old zQ175DN het and wt mice for characterization of its pharmacokinetic properties and
150 monitored its stability in the brain and plasma (Fig. S3A).

151 Radio-high-performance liquid chromatography (radio-HPLC) coupled with γ -counter
152 measurement of mouse brain homogenates and plasma samples did not show [¹¹C]CHDI-180R-
153 related metabolites in zQ175DN mice independent of genotype and mHTT inclusion amount (4-
154 and 10-month-old het) (Fig. S3B,C). Next, to evaluate [¹¹C]CHDI-180R kinetics, we performed
155 90-min dynamic microPET scans following intravenous injection. We extracted an image-derived
156 input function (IDIF) (Fig. S3E) from the heart blood pool of each animal to serve as a non-
157 invasive input function (24, 25). Injection of [¹¹C]CHDI-180R (Table S1) resulted in a rapid
158 radioactive uptake in the brain with standardized uptake value (SUV, regional radioactivity
159 normalized to the injected activity and body weight) showing genotypic difference over the 90-
160 min period and reversible kinetics described by a two-tissue compartment model (2TCM) (Fig.
161 S3F, Table S2). The resulting striatal total volume of distribution using IDIF (V_T (IDIF) as a surrogate
162 of V_T (26)) in het zQ175DN was significantly increased by 62% compared to wt littermates (Fig.
163 S3G, $P < 0.0001$) with extremely low coefficients of variation (wt=2.84%, het=5.2%; Fig. S3G).
164 Scan acquisition could be reduced from 90-min down to 60-min (Fig. S3H, $R^2 = 0.99$, $P < 0.0001$),

165 and reliable V_T (IDIF) estimation of [^{11}C]CHDI-180R binding was also obtained using the Logan
166 graphical analysis (27) as demonstrated by the optimal linear relationship ($y=1.08x-0.04$) with V_T
167 (IDIF) estimation using 2TCM (Fig. S3I, $R^2=0.99$, $P<0.0001$). Finally, V_T (IDIF) parametric maps of
168 [^{11}C]CHDI-180R using the Logan model could be generated for both zQ175DN wt and het mice
169 (Fig. S3J).

170

171 **Longitudinal characterization of [^{11}C]CHDI-180R PET ligand allows detection of temporal** 172 **dynamics of mHTT pathology**

173 We performed a longitudinal evaluation of [^{11}C]CHDI-180R microPET imaging in zQ175DN het
174 and wt mice (Fig. 2A; Table S3). In zQ175DN, mHTT-containing inclusions initiate in striatum
175 (20), and indeed the striatum was the first region where significant V_T (IDIF) differences were
176 detected at 3 months of age (Fig. 2B,C, $P<0.001$). [^{11}C]CHDI-180R V_T (IDIF) values revealed stable
177 values over time in wt mice given the lack of specific target, whereas het zQ175DN displayed a
178 significant temporal increase in all brain regions (striatum, 6.7% ($P<0.001$), 40.3% ($P<0.0001$),
179 63.1% ($P<0.0001$), and 81.3% ($P<0.0001$), at 3, 6, 9 and 13 months of age, respectively) (Fig.
180 2C). For sample size requirements in therapeutic studies in het zQ175DN mice, see Table S4. The
181 increasing [^{11}C]CHDI-180R binding within zQ175DN het was also confirmed by the voxel-based
182 analysis of [^{11}C]CHDI-180R V_T (IDIF) parametric maps, which could also identify specific cortical
183 clusters of increased binding at advanced disease (13m > 9m) (Fig. 2D).

184 We monitored mHTT inclusions by mEM48 and 2B4 (28) immunoreactivity (Fig. 2A). In line
185 with the [^{11}C]CHDI-180R microPET findings, striatal mHTT inclusions could be observed starting
186 at 3 months of age with a significant increase in size with disease progression in het zQ175DN
187 mice for both mEM48 (Fig. 2E,F, $P<0.0001$) and 2B4 (28) (Fig. 2G,H, $P<0.0001$), Whereas no
188 mHTT inclusion was detected in wt littermates (Fig. S4).

189 Within the CNS, mHTT inclusions are not limited to the brain as they may be found in the spinal
190 cord in human patients(29). In the cervical spinal cord of zQ175DN het mice, [^{11}C]CHDI-180R
191 binding was significantly increased compared to wt littermates (Fig. 2I, $P<0.001$) as also
192 confirmed by [^3H]CHDI-180 ARG (Fig. 2J,K, $P<0.0001$) and mEM48 immunostaining (Fig. 2L,
193 $P<0.0001$).

194

195 **[¹¹C]CHDI-180R imaging identifies time- and region-dependent changes in mHTT**
196 **pathology after virally-mediated, mHTT-selective striatal knockdown in the zQ175DN**
197 **model**

198 Given the ability of [¹¹C]CHDI-180R to detect the temporal evolution of the mHTT pathology in
199 live animals, we examined its applicability in measuring the effect of local or global mHTT
200 lowering strategies (Fig. 3A, 4A, 5B; Tables S5-S9). We have previously demonstrated that striatal
201 ZFP-mediated mHTT repression could improve molecular, histopathological, and
202 electrophysiological deficits in the zQ175 het mice (12). In this work, we used the ZFP-D repressor
203 driven by the human synapsin promoter (12) in two experimental paradigms to assess binding
204 changes when the treatment is administered prior to disease onset (early treatment) compared to
205 administration after disease symptoms are well manifested (late treatment) (12-14) (Fig. 3A, 4A).
206 Het zQ175DN or wt mice were injected into striata with either AAV ZFP (treatment), ZFP lacking
207 the DNA-binding domain (ZFP-ΔDBD; control), or vehicle (PBS) before (2 months of age) or
208 after (5 months of age) the age of mHTT inclusion formation and disease onset (13, 14) (Fig. 3B,
209 4B). As shown in Figure 3B, we designed the experiment in a way that each animal acts as its own
210 control; in one cohort, zQ175DN mice are injected with active ZFP in the left hemisphere, and
211 with an inactive ZFP-ΔDBD in the right hemisphere. A second cohort of zQ175DN mice and a
212 cohort of wild-type mice were injected with the vehicle in the left hemisphere, to control for the
213 potential impact of viral transduction and exogenous protein expression, and with the control ZFP-
214 ΔDBD in the right hemisphere. Animals were monitored longitudinally via [¹¹C]CHDI-180R PET.
215 In addition, other biomarkers known to undergo early, progressive, and profound changes years
216 before clinical diagnosis, PDE10a, D₁R, and D_{2/3}R (15, 17, 30-32), were assessed longitudinally
217 using [¹⁸F]MNI-659, [¹¹C]SCH23390, and [¹¹C]Raclopride, respectively (Tables S5,S6). In the
218 early intervention paradigm, mHTT pathology and PDE10a were assessed in vivo. During the late
219 intervention paradigm, one study cohort was imaged for mHTT pathology and PDE10a, whereas
220 a second cohort was analyzed for D₁R and D_{2/3}R. At the study end, in vivo findings were
221 corroborated by ARG and immunostaining. Progressive alterations in these markers are
222 recapitulated in zQ175DN het mice (8, 12, 16, 33-35).

223 In the early ZFP intervention (Fig. 3A,B; Tables S5 and S8), [¹¹C]CHDI-180R V_T (IDIF) values for
224 the ZFP- versus ΔDBD-injected striatum were significantly reduced by 2.8, 9.0, and 16.3% at 3,
225 6, and 10 months of age, respectively (Fig. 3C,E; treatment effect: $P < 0.0001$). No difference was
226 observed for control zQ175DN cohorts (Fig. 3C,E; Fig. S5A,B). The reduced [¹¹C]CHDI-180R
227 binding was paralleled by a significant increase in the non-displaceable binding potential (BP_{ND} ,
228 a quantitative index of receptor density (26)) for [¹⁸F]MNI-659 (22.7%, 98.1%, and 98.1% at 3, 6,
229 and 10 months of age, respectively, treatment effect: $P < 0.0001$; or 1-, 4- and 8 months after viral
230 transduction with ZFP-mediated mHTT suppression), with no contralateral difference for the
231 control zQ175DN cohorts (Fig. 3D,F; Fig. S5C,D). The estimated “therapeutic” effect for the early
232 or late intervention was calculated according to eq. 1 (See Materials and Methods) as the difference
233 in het mice between ZFP-treated hemisphere and control ΔDBD-injected hemisphere. This
234 difference was normalized to the total genotypic difference, estimated as the delta between ΔDBD-
235 injected striatum in wt and het mice. The resulting estimate suggested approximately 40% mHTT
236 lowering (42.2, 40.6, and 38.8% at 3, 6, and 10 months of age), which was positively associated
237 with the 43.3% PDE10a preservation in the same animals (Fig. 3G; $R^2 = 0.52$, $P < 0.0001$). Upon
238 completion of the studies, ARG was performed using [³H]CHDI-180 (mHTT), [³H]SCH23390
239 (D_1R), and [³H]Raclopride ($D_{2/3}R$) as well as immunostaining for PDE10a. Striatal [³H]CHDI-180
240 binding for the ZFP- versus ΔDBD-injected striatum was significantly reduced by 53.6% (Fig.
241 3H,I, $P < 0.0001$), showing correlation with the in vivo [¹¹C]CHDI-180R PET measurement (Fig.
242 3J; $R^2 = 0.67$, $P < 0.0001$). A significant increase in ZFP- versus ΔDBD-injected striatum was
243 measured for PDE10a immunostaining (30.7%, $F_{(2,30)} = 59.40$, $P < 0.0001$), D_1R with
244 [³H]SCH23390 (40.6%, $F_{(2,30)} = 34.98$, $P < 0.0001$), and $D_{2/3}R$ with [³H]Raclopride (10.9%,
245 $F_{(2,30)} = 6.59$, $P < 0.01$) (Fig. 3K-M). Noteworthy, the reduction in mHTT amount was correlated
246 with preservation of all measured striatal markers (PDE10a: $R^2 = 0.84$, $P < 0.0001$; D_1R : $R^2 = 0.79$,
247 $P < 0.0001$; $D_{2/3}R$: $R^2 = 0.29$, $P = 0.0012$; Fig. S6).

248 In the late ZFP intervention paradigm (Fig. 4A,B; Tables S6 and S9), [¹¹C]CHDI-180R V_T (IDIF)
249 values for the ZFP- versus ΔDBD-injected striatum were significantly reduced by 4.3% and 10.3%
250 at 6 and 10 months of age ($P < 0.0001$, 1 month and 5 months post viral transduction), respectively,
251 without contralateral differences for control zQ175DN cohorts (Fig. 4C,G; Fig. S7A,B). In
252 addition, a significant increase in BP_{ND} for ZFP- compared to ΔDBD-ZFP injected striatum was

253 measured for all translational biomarkers, with [¹⁸F]MNI-659 being increased by 20.4% and 43.6%
254 (Fig. 4D,H; Fig. S7C,D), [¹¹C]SCH23390 by 7.4% and 17.4% (Fig. 4E,I; Fig. S7E,F), and
255 [¹¹C]Raclopride by 8.9% and 14.1% (Fig. 4F,J; Fig. S7G,H) at 6 and 10 months, respectively
256 (treatment effect: $P < 0.0001$ for all markers). However, when the percentage difference in BP_{ND}
257 between hemisphere was corrected by the het control group, the ZFP group displayed increased
258 binding of 19.3% and 38.7% ([¹⁸F]MNI-659), by 1.7% and 9.6% ([¹¹C]SCH23390), and by 4.5%
259 and 4.2% ([¹¹C]Raclopride) at 6 and 10 months, respectively (Fig. 4H-J, treatment effect:
260 $P < 0.0001$ for all markers). The estimated therapeutic effect for the late intervention, (eq. 1),
261 indicated approximately 23% mHTT lowering (19.4% and 23.6% at 6 and 10 months of age),
262 positively associated to the 25.5% PDE10a preservation (Fig. 4K; $R^2 = 0.26$, $P = 0.002$). In post-
263 mortem experiments, [³H]CHDI-180 binding for the ZFP- versus Δ DBD-injected striatum was
264 significantly reduced by 42.1% ($F_{(2,73)} = 116.5$, $P < 0.0001$) (Fig. 4L,M), showing agreement with
265 [¹¹C]CHDI-180R (Fig. 4N; $R^2 = 0.56$, $P = 0.0003$). This effect was lower than the 53.6% measured
266 during early intervention (Fig. 3I), possibly due to time of intervention (2 or 5 months of age), the
267 duration of the treatment (8 months or 5 months), or a combination of these factors. Additionally,
268 we observed a significant increase in ZFP- versus Δ DBD-injected striatum for PDE10a (12.8%,
269 $F_{(2,63)} = 52.75$, $P < 0.0001$), D₁R with [³H]SCH23390 (25.6%, $F_{(2,66)} = 37.70$, $P < 0.0001$), and D_{2/3}R
270 with [³H]Raclopride (6.5%, $F_{(2,66)} = 3.71$, $P = 0.0297$) (Fig. 4O-Q). The preservation of all measured
271 striatal markers in the ZFP-injected hemisphere was correlated with the reduction in mHTT protein
272 species (PDE10a: $R^2 = 0.61$, $P < 0.0001$; D₁R: $R^2 = 0.48$, $P < 0.0001$; D_{2/3}R: $R^2 = 0.14$, $P = 0.0016$; Fig.
273 S6 and S8).

274 Meso Scale Discovery (MSD) measurements showed that ZFP treatment did not alter wt mouse
275 HTT concentration (detected using the combination of mouse-specific mAb 2133 & the D7F7
276 mAb), but significantly decreased the amount of soluble and aggregated mHTT in both the early
277 (39% and 69%, respectively; $P < 0.0001$, Fig. S9A-C) and late (43% and 37%, respectively; $P < 0.05$,
278 Fig. S9D-F) intervention studies. Soluble expanded HTT protein was detected using 2B7-MW1
279 assay (36) and aggregated mHTT was detected using MW8-4C9 assay (37). Most likely, mHTT
280 reduction on a level of only ZFP expressing cells would be higher since we measured an average
281 of 38% AAV-ZFP transduced cells along the rostro-caudal axis, following AAV ZFP and Δ DBD-
282 ZFP injections (Fig. S10). We analyzed several brains to confirm the extent of ZFP distribution
283 and its impact on mHTT aggregate number and intensity using mEM48 immunohistochemistry.

284 In the early treatment paradigm, the striatal region expressing the AAV ZFP treatment did not
285 display any mHTT nuclear inclusions at 10 months of age (8 months of treatment) unlike the ZFP
286 non-transduced region or contralateral Δ DBD-ZFP injected hemisphere (Fig. S11A,B). In contrast,
287 in the late treatment paradigm, smaller and fewer intranuclear mHTT inclusions are present
288 following the AAV ZFP treatment than in the ZFP non-transduced area or the contralateral Δ DBD-
289 ZFP injected hemisphere (Fig. S11C,D). No evidence of microglial or astrocytic reactivity in the
290 striatum of injected animals, as judged by Iba1 and GFAP reactivity (Fig. S12), recapitulating what
291 we reported in Zeitler et al (12).

292 Collectively, these observations suggest that we achieve a 40% mHTT reduction in the early
293 intervention paradigm and that this value is determined by the extent of neuronal transduction and
294 viral distribution in the mouse striatum (38%). This value is in concordance with the 38.9% signal
295 decrease, measured in vivo using PET, with [11 C]CHDI-180R. In contrast, in the late intervention
296 paradigm, and consistent with residual pre-existing aggregate pathology that remains after AAV-
297 ZFP administration after disease onset, we only achieved a 23.6% therapeutic effect as measured
298 in vivo with [11 C]CHDI-180R at 10 months of age.

299

300 [11 C]CHDI-180R PET imaging detects widespread suppression of mHTT in the regulatable 301 mHTT knock-in LacQ140^I(*) mouse model

302 Current clinical HTT-lowering directed therapeutic strategies are seeking to explore what degree
303 of HTT reduction may produce clinical benefit in cortical and striatal regions, with several clinical
304 programs targeting a 50% reduction (5, 6, 11, 38, 39). Therefore, we wanted to detect CNS-wide
305 changes in mHTT within the range being pursued clinically, using a newly characterized knock-
306 in LacQ140^I(*) mouse model, which allows for mHTT lowering in a regulatable fashion to
307 approximately 40-50% throughout the body in a Q140 KI context (40). Due to the presence of the
308 LacO repressor binding sites, the exposure to IPTG (isopropyl- β -d-1-thiogalactopyranoside)
309 enables (derepresses) the expression of mHTT. Upon withdrawal of IPTG, mHTT expression is
310 suppressed throughout the organism (Fig. 5; Fig. S9G-I). The extent of mHTT aggregated species,
311 as judged by MSD assays with MW8-4C9 (Fig. S9H) depends on the timing of mHTT mRNA
312 suppression.

313 We employed this model to lower *mHtt* systemically at 2 or 8 months of age, before and after
314 mHTT inclusion formation and disease onset, and compared them to control mice or LacQ140^I(*)
315 mice with *mHtt* expressed throughout its life, at 13 months of age (Fig. 5A,B; Tables S7).
316 [¹¹C]CHDI-180R V_T (IDIF) values were reduced consistently with suppression duration in all brain
317 regions examined following IPTG withdrawal before (2-13 months) and after (8-13 months)
318 mHTT inclusion formation (Fig. 5C,D). The estimated mHTT suppression effect was calculated
319 according to eq. 2 (See Materials and Methods) as the difference between het mice subjected to
320 *mHtt* lowering (either as of 2 or 8 months) and het mice without *mHtt* suppression. This difference
321 was normalized to the total genotypic difference, estimated as the delta between het, no
322 suppression (total signal) and wt, no suppression mice (non-displaceable signal). We estimated a
323 global 80-95% or 20-35% mHTT aggregate lowering following IPTG withdrawal at 2 or 8 months
324 (treatment effect striatum: $F_{(3,48)}=62.30$, $P<0.0001$). The apparent disconnect between the 40-50%
325 *mHtt* lowering in this model and the 80-95% mHTT lowering measured with [¹¹C]CHDI-180R in
326 the early intervention study suggests that a modulation of 40-50% of *mHtt* expression prior to
327 aggregate formation might be sufficient to largely avoid or delay the generation of [¹¹C]CHDI-
328 180R-binding species.

329 Consistently, autoradiographic [³H]CHDI-180 binding was significantly reduced (Fig. 5E,F;
330 striatum, $F_{(3,47)}=133.80$, $P<0.0001$) demonstrating agreement with [¹¹C]CHDI-180R PET (Fig.
331 5G, $R^2=0.779$, $P<0.0001$). The extent of mHTT lowering was supported by mEM48
332 immunostaining (Fig. 5H,I; $F_{(3,46)}=360.80$, $P<0.0001$), in line with the [¹¹C]CHDI-180R binding
333 (Fig. 5J, $R^2=0.794$, $P<0.0001$), as well as MSD measurements of HTT using cerebellar extracts
334 obtained from the same animals (Fig. S9G-I; $P<0.05$ - $P<0.0001$).

335

336

337

338 **DISCUSSION**

339 Several therapeutic studies targeting HTT expression are being evaluated or planned in clinical
340 studies (5, 6, 11, 38, 39). Given the different therapeutic modalities leading to distinct restricted
341 distribution patterns, an understanding of the regional effects of HTT lowering agents is

342 fundamental for interpreting, and improving upon, clinical trial results. It is in this context that we
343 set out to develop a strategy to identify and characterize potential indicators that can help guide
344 the clinical development of HTT lowering agents. Here we extend our prior characterization of
345 CHDI-180R and demonstrate the time- and region-dependent appearance of mHTT pathology in
346 the HD mouse models R6/2, HdhQ80, and zQ175DN. The ligand is suitable to detect genotype
347 and region-specific differences in mHTT pathology throughout the brain, allowing for its
348 deployment in therapeutic studies with manageable sample size and a longitudinal manner. We
349 were able to ascertain different regional pathology within the striatum, particularly in HdhQ80
350 mice, which appears to proceed from a ventral to dorsal trajectory, an observation reminiscent of
351 human pathology that proceeds caudal-to-rostral and dorsal-to-ventral (2, 3).

352 We applied [¹¹C]CHDI-180R in two interventional paradigms when mHTT is lowered in a
353 restricted manner in the striatum of mice, or more broadly throughout the mouse brain, within the
354 range of mHTT suppression expected in clinical studies (~50%). The extent of lowering detected
355 by [¹¹C]CHDI-180R correlates well with the extent of mHTT suppression as measured by
356 quantitative assays for soluble and aggregated forms of mHTT. These studies show that
357 [¹¹C]CHDI-180R could potentially be used irrespective of the regional distribution of the
358 therapeutic agents or the extent of lowering. Furthermore, we verified the extent of lowering by
359 ARG, showing excellent concordance with PET imaging. In the context of the ZFP repressor, the
360 decrease in the signal obtained with [¹¹C]CHDI-180R appears rapid (1-month post administration
361 of AAV-ZFP), and is sustained during the duration of the studies (up to 8 months). When
362 administered early, prior to the appearance of pathology, AAV-ZFP prevents mHTT inclusion and
363 extranuclear aggregation, and the decrease of the signal detected by [¹¹C]CHDI-180R might be
364 explained by the extent of agent distribution and neuronal transduction (in our case, about 40% of
365 the striatum).

366 A number of considerations and limitations should be highlighted to appropriately interpret the
367 findings. First, we do not yet have a full understanding of the various species of mHTT that
368 constitute the binding site(s) for CHDI-180. Nonetheless, based on previous in vitro studies (8, 9),
369 we know this ligand can bind oligomerized and some forms of fibrillar mHTT but not to
370 monomeric soluble HTT. Besides our poor understanding of the precise states of mHTT to which
371 CHDI-180 binds to, adequate information on the dynamics between the soluble and aggregated
372 pools of mHTT is similarly lacking. We expect that the availability of this PET tracer in parallel

373 to biofluid readouts for HTT, like mass spectrometry and quantitative MSD/Single Molecule
374 Counting, may facilitate a better understanding of how these different pools of mHTT are handled
375 in brain cells, and how the extent of mHTT lowering may shift the dynamics of such cellular
376 processes. Second, mHTT concentration have been measured clinically using a 2B7/MW1
377 immunoassay (5), therefore, comparing the extent of lowering of soluble amount of mHTT using
378 2B7/MW1 in CSF to the spinal mHTT as well as the extent of parenchymal changes observed with
379 [¹¹C]CHDI-180R would be desirable. However, method development for mouse CSF mHTT
380 detection remains difficult and samples were not collected in this work. However, a disconnect
381 between the extent of lowering of mHTT in CSF as compared to caudate/putamen suppression
382 concentration after AAV5-AMT130 administration was recently shown in a mHTT transgenic
383 minipig model (7). Third, mHTT accumulates in all brain structures thus measurement of input
384 function for [¹¹C]CHDI-180R quantification is necessary. Since arterial blood sampling in mice
385 represents a very challenging and end-of-life procedure, we exploited the use of a cardiac IDIF for
386 non-invasive quantification (24, 41). Although this approach might be sensitive to over- or under-
387 estimation of the blood activity (42), it is suitable to perform reliable comparative studies as shown
388 in previous work (43-45) as well as indicated by the measurement stability in same animals over
389 time and confirmed across different studies. Importantly, this limitation will not apply to larger
390 animal models and humans, where arterial blood sampling is feasible. Fourth, PET imaging of
391 mHTT density was measured with V_T , which comprises both specific and non-displaceable
392 binding, whereas PDE10a, D₁R, and D_{2/3}R could be quantified with BP_{ND} , a direct measure of
393 target density, given the presence of a reference region (26). Therefore, any change measured in
394 V_T is intrinsically smaller than with BP_{ND} , an important aspect to consider for adequate comparison
395 across markers. Overall, given the long half-life of mHTT protein and the impact that pre-existing
396 aggregate pathology can have in establishing an adequate experimental design, future studies will
397 be needed to obtain a detailed understanding of the effects of different therapeutic agents targeting
398 mHTT DNA or RNA on both soluble and aggregated amounts in terms of type, timing, and
399 magnitude of responsiveness during the disease course.

400 We investigated potential striatal markers that can serve as markers of functional SPN restoration.
401 Several PET ligands, previously shown to track disease progression in HD individuals, have been
402 shown to track progression in models of HD (33-35, 44, 46). We show that the response to mHTT
403 lowering in SPNs is fast and durable, and that these effects can be observed even in the context of

404 established disease and aging, at least in the zQ175DN model. During the early intervention
405 paradigm, all striatal markers responded within a month of therapy, suggesting an improvement of
406 cellular alterations in indirect-pathway SPNs (expressing both PDE10 and D₂R), and direct-
407 pathway neurons (expressing PDE10 and D₁R). When AAV-ZFP is administered after disease
408 onset, the response is more muted, but present for all tracers, particularly as judged by ARG, which
409 has a higher signal to background ratio than microPET. PDE10a and D₁R expression appear more
410 responsive to mHTT lowering than D_{2/3}R, arguing that direct pathway neurons (affected later in
411 the disease) might be more amenable to functional restoration.

412 The strong correlation seen in intra-animal comparisons between [¹¹C]CHDI-180R and PDE10a
413 binding across our cohorts strongly supports the concept that PDE10a imaging may be a sensitive
414 translational marker of early therapeutic benefit, whether from mHTT lowering or any other
415 intervention that restores striatal projection function. As this marker is one of the earliest markers
416 altered in premanifest individuals, including those far from disease onset (15-17), PDE10a imaging
417 can be used to track functional responses to HTT lowering in prodromal clinical studies.

418 In summary, we demonstrated the development of a small-molecule PET ligand with high affinity
419 and selectivity for mHTT to monitor non-invasively mHTT pathology in the living brain and track
420 region- and time-dependent suppression of mHTT amount in response to therapeutic intervention.
421 We also showed that therapeutic agents, such as AAV-ZFP, can be functionally restorative and
422 their effects can be measured by the preservation of striatal imaging markers. The ability to
423 measure time and region-specific effects of agents that suppress HTT expression will be extremely
424 informative to understand the pharmacodynamic effects and clinical impact of experimental gene
425 therapy and small molecule agents being evaluated in clinical trials.

426

427 **MATERIALS AND METHODS**

428 **Study design**

429 The objective of this study was to investigate the utility of the high affinity and selectivity mHTT
430 PET ligand [¹¹C]CHDI-180R to detect mHTT aggregation in affected brain cells and its application
431 as indicator of pharmacological activity of agents that target HTT expression in the living brain.
432 We first performed ARG and IHC analysis on brain samples from post-mortem human tissue as
433 well as zQ175DN, HdhQ80, and R6/2 HD models and age-matched wt mice to explore signal
434 concentration and pattern. Next, we carried out a longitudinal study to characterize [¹¹C]CHDI-
435 180R PET imaging to enable non-invasive monitoring of mHTT pathology in the brain and spinal
436 cord of untreated wt and het zQ175DN mice. This work was used to quantify [¹¹C]CHDI-180R
437 binding at different disease stages and perform power analysis for adequate sample sizes in
438 therapeutic interventions lowering mHTT concentration. With the aim of determining whether
439 [¹¹C]CHDI-180R could track region- and time-dependent suppression of mHTT in response to
440 therapeutic interventions targeting mHTT expression, we performed longitudinal studies in
441 zQ175DN mice with a ZFP-based therapeutic intervention as well as in the regulatable
442 LacQ140^l(*) mouse model. The sample size was calculated for all in vivo cross-sectional and
443 longitudinal studies to provide 80% statistical power with a type 1 error rate of 0.05 in detecting
444 changes of PET imaging readouts. No prior power analysis was performed for in vitro studies, but
445 sample size resulted to be adequate for the aim of the analyses. Investigators performing the
446 longitudinal therapeutic studies were blinded to treatment condition until completion of studies.
447 Randomization was applied to each experiment. No samples correctly acquired were excluded
448 from the study.

449

450

451 **PET imaging**

452 *Image acquisition*

453 Dynamic microPET/Computed tomography (CT) images were acquired using two virtually
454 identical Siemens Inveon PET/CT scanners (Siemens Preclinical Solution) as previously described
455 (41, 45, 47). Animals were anesthetized using isoflurane in medical oxygen (induction 5%,
456 maintenance 1.5%) and catheterized in the tail vein for intravenous (i.v.) bolus injection of the

457 tracer. Animals were placed on the scanner bed with the full body in the PET scanner's field of
458 view (FOV) to allow the extraction of the image-derived input function (IDIF) from the left
459 ventricle as previously described (24, 25). Bolus injection of radiotracer occurred over a 12-second
460 interval (1 ml/min) using an automated pump (Pump 11 Elite, Harvard Apparatus) at the onset of
461 the dynamic microPET scan. Information regarding molar activity injected radioactivity, injected
462 mass, body weight, and age on scan day for each radioligand at different time points and studies
463 are reported in Tables S1, S4, S5-S7. Radioligands were injected with activity as high as possible
464 to obtain good image quality and keeping the cold mass as low as possible in order not to violate
465 tracer conditions. We experimentally measured and characterized the mass-dose effect for the
466 various tracers. In all experimental paradigms we stayed well below the critical limit and set our
467 target at 1.25 $\mu\text{g}/\text{kg}$ for [^{11}C]CHDI-180R, 1 $\mu\text{g}/\text{kg}$ for [^{18}F]MNI-659, 2 $\mu\text{g}/\text{kg}$ for [^{11}C]SCH23390,
468 1.5 $\mu\text{g}/\text{kg}$ for [^{11}C]Raclopride. PET data were acquired in list mode format. Dynamic scans lasted
469 60 min for [^{11}C]CHDI-180R and [^{11}C]Raclopride, whereas a 90 min acquisition was performed
470 for [^{18}F]MNI-659 and [^{11}C]SCH23390. PET scans were followed by a 10 min 80 kV/500 μA CT
471 scan on the same gantry for attenuation correction and coregistration purposes. Acquired PET data
472 were reconstructed into 33 or 39 (for 60 or 90 min acquisition, respectively) frames of increasing
473 length (12x10s, 3x20s, 3x30s, 3x60s, 3x150s, and 9 or 15x300s) using a list-mode iterative
474 reconstruction with proprietary spatially variant resolution modeling in 8 iterations and 16 subsets
475 of the 3D ordered subset expectation maximization (OSEM 3D) algorithm (48). Normalization,
476 dead time, and CT-based attenuation corrections were applied. PET image frames were
477 reconstructed on a 128x128x159 grid with 0.776x0.776x0.796 mm^3 voxels.

478

479 ***Image processing***

480 Image analysis was performed with PMOD 3.6 software (Pmod Technologies) applying a CT-
481 based pipeline for the longitudinal natural history study and an MR-based pipeline for the
482 therapeutic and LacQ140^I(*) studies. When we applied the CT-based pipeline, spatial
483 normalization of the PET/CT images was done through brain normalization of the CT image to
484 the CT/MRI template with predefined volumes-of-interest (VOIs) adapting the previously
485 described procedure (34). The spatial transformations were applied to the dynamic PET images
486 and assessed for accuracy following spatial transformation. Using the VOI template adapted from
487 the Waxholm atlas (49) (as shown in Fig. S3), time-activity curves (TACs) for the striatum, motor

488 cortex, hippocampus, thalamus, and cerebellum were extracted from the dynamic PET images to
489 perform kinetic modeling.

490 Since we previously observed that the use of magnetic resonance imaging (MRI) templates for
491 spatial normalization and VOI definition improves the accuracy of the regional quantification of
492 PET data with focal uptake, the therapeutic and LacQ140^I(*) studies were processed using an MR-
493 based pipeline (34). VOIs were manually adapted from the Waxholm atlas (49) to match each
494 genotype and age-specific MR template. TACs for the striatum, motor cortex, hippocampus,
495 thalamus, and cerebellum were extracted from the dynamic PET images in order to perform kinetic
496 modeling. For analysis of spinal cord, VOIs were manually drawn on the individual CT images,
497 and TACs were extracted from the dynamic scans for regional quantification.

498

499 ***Kinetic modeling***

500 In zQ175DN and Q140 mouse models, mHTT accumulates in all brain structures (8, 14, 20, 40)
501 and no suitable reference region for relative quantification could be identified. Hence absolute
502 quantification for [¹¹C]CHDI-180R was performed to calculate the total volume of distribution
503 based on image-derived input function (V_T (IDIF)) as a non-invasive surrogate of the V_T . Kinetic
504 modeling fitted regional TACs using the Logan model (27) and the image-derived input function
505 (IDIF) with the start of the linear regression (t^*) calculated according to the maximum error
506 criterion of 10%. The IDIF was obtained from the whole blood activity derived from the PET
507 images by generating a region-of-interest (threshold-based 50% of max) in the lumen of the left
508 ventricle as previously described (24, 41). Since only negligible metabolism of [¹¹C]CHDI-180R
509 was observed in different genotypes and ages (parent compound >95%), no correction for
510 radiometabolites was applied.

511 Parametric V_T (IDIF) maps were generated through voxel-based graphical analysis (Logan) (27)
512 using the IDIF as input function, and were then cropped using the brain mask of the MRI template,
513 represented as group averages, and overlaid onto a 3D mouse brain template for anatomical
514 reference. Individual images were smoothed with an isotropic gaussian filter (0.5 mm in full width
515 at half maximum). For the longitudinal natural history study, voxel-based analysis with Statistical
516 Parametric Mapping (SPM) using SPM12 (Wellcome Centre for Human Neuroimaging) was
517 performed on het zQ175DN mice to evaluate the voxel-based changes with disease progression.
518 Data from zQ175DN het mice were compared between time points in order to determine

519 longitudinal changes in [¹¹C]CHDI-180R V_T (IDIF). Statistical t maps were generated for a peak
520 voxel threshold of $P=0.01$ (uncorrected) and a cluster threshold of 10 voxels (0.8 mm³). Only
521 significant clusters with $P<0.01$ were considered.

522 For the quantification of [¹⁸F]MNI-659, [¹¹C]SCH23390, and [¹¹C]Raclopride the binding
523 potential (BP_{ND}) was determined by fitting the regional TACs using the simplified reference tissue
524 modeling (SRTM) (50). The striatum was selected as the receptor-rich region and the cerebellum
525 the receptor-free region (reference region) (34, 47). Parametric BP_{ND} maps were generated using
526 SRTM2 (51) with the k_2' as calculated with SRTM (50). The individual images were smoothed
527 with an isotropic gaussian filter (0.5 mm in full width at half maximum), cropped using the brain
528 mask of the MRI template, represented as group averages, and overlaid onto each condition- and
529 age-specific 3D brain template for anatomical reference.

530 Since ZFP delivery was restricted to the ipsilateral striatum, the therapeutic response of each
531 molecular target in the early and late ZFP intervention studies was estimated as follows according
532 to Fig. 3B and 4B:

$$533 \text{ Therapeutic response (\%)} = \frac{ZFP_{(LSTR \text{ treated } het)} - \Delta DBD_{(RSTR \text{ treated } het)}}{\Delta DBD_{(wt)} - \Delta DBD_{(RSTR \text{ treated \& control } het)}} * 100 \quad \text{eq. 1}$$

534 Where LSTR and RSTR represent the left and right striatum, respectively.

535 In the LacQ140^l(*) studies, the mHTT lowering response of [¹¹C]CHDI-180R was estimated as
536 follows:

$$537 \text{ mHTT lowering response (\%)} = \frac{HET_{(2\text{-or } 8\text{-} 13m \text{ supp})} - HET_{(no \text{ supp})}}{HET_{(no \text{ supp})} - WT_{(no \text{ supp})}} * 100 \quad \text{eq. 2}$$

538

539

540 **Statistical analysis**

541 Statistical analysis was performed in GraphPad Prism v9.1 (GraphPad Software) and JMP Pro 14
542 (SAS Institute Inc.). Data are expressed as the mean \pm standard deviation (s.d.) unless otherwise
543 indicated in the figure legends. To choose the appropriate statistical test, data were checked for
544 normality using the Shapiro-Wilk test. If the normality test was not passed, non-parametric
545 statistical tests were used. Longitudinal analysis of each PET readout was performed using linear
546 mixed-effects models with each radioligand quantification as the primary endpoint. Genotype,
547 cohort, time point, region, and treatment (when applicable) as fixed factors, with subjects as a
548 random effect. Interaction effects (genotype*time, cohort*time, treatment*time, and

549 treatment*region) were evaluated as well. Comparisons were performed to evaluate regional
550 temporal and genotypic differences as well as treatment effects. Correlation coefficients were
551 calculated with Pearson's correlation analysis. Sample size calculations at desired therapeutic
552 effects were performed in G*Power software (<http://www.gpower.hhu.de/>). Statistical significance
553 was set at $P < 0.05$, with the following standard abbreviations used to reference P values: ns, not
554 significant; * $P < 0.05$; ** $P < 0.01$; *** $P < 0.001$; **** $P < 0.0001$. Detailed statistical information for
555 each experiment is provided in the corresponding figure legends.

556

557 **Supplementary Materials**

558 Materials and Methods

559 Figs. S1 – S10

560 Tables S1 – S12

561 Datafile S1: Raw data

562

563

564 **References**

565 1. T. H. s. D. C. R. Group, A novel gene containing a trinucleotide repeat that is expanded and unstable on
566 Huntington's disease chromosomes. The Huntington's Disease Collaborative Research Group. *Cell* **72**, 971-
567 983 (1993).

568 2. H. J. Waldvogel, E. H. Kim, L. J. Tippett, J. P. Vonsattel, R. L. Faull, The neuropathology of Huntington's
569 disease. *Curr Top Behav Neurosci* **22**, 33-80 (2015).

570 3. U. Rub, J. P. Vonsattel, H. Heinsen, H. W. Korf, The Neuropathology of Huntington s disease: classical
571 findings, recent developments and correlation to functional neuroanatomy. *Adv Anat Embryol Cell Biol*
572 **217**, 1-146 (2015).

573 4. H. B. Kordasiewicz, L. M. Stanek, E. V. Wancewicz, C. Mazur, M. M. McAlonis, K. A. Pytel, J. W.
574 Artates, A. Weiss, S. H. Cheng, L. S. Shihabuddin, G. Hung, C. F. Bennett, D. W. Cleveland, Sustained
575 therapeutic reversal of Huntington's disease by transient repression of huntingtin synthesis. *Neuron* **74**,
576 1031-1044 (2012).

577 5. S. J. Tabrizi, B. R. Leavitt, G. B. Landwehrmeyer, E. J. Wild, C. Saft, R. A. Barker, N. F. Blair, D.
578 Craufurd, J. Priller, H. Rickards, A. Rosser, H. B. Kordasiewicz, C. Czech, E. E. Swayze, D. A. Norris, T.
579 Baumann, I. Gerlach, S. A. Schobel, E. Paz, A. V. Smith, C. F. Bennett, R. M. Lane, I.-H. S. S. T. Phase 1-
580 2a, Targeting Huntingtin Expression in Patients with Huntington's Disease. *N Engl J Med* **380**, 2307-2316
581 (2019).

582 6. E. A. Spronck, A. Valles, M. H. Lampen, P. S. Montenegro-Miranda, S. Keskin, L. Heijink, M. M. Evers,
583 H. Petry, S. J. V. Deventer, P. Konstantinova, M. Haan, Intraatrial Administration of AAV5-miHTT in
584 Non-Human Primates and Rats Is Well Tolerated and Results in miHTT Transgene Expression in Key
585 Areas of Huntington Disease Pathology. *Brain Sci* **11**, (2021).

586 7. A. Valles, M. M. Evers, A. Stam, M. Sogorb-Gonzalez, C. Brouwers, C. Vendrell-Tornero, S. Acar-
587 Broekmans, L. Paerels, J. Klima, B. Bohuslavova, R. Pintauro, V. Fodale, A. Bresciani, R. Liscak, D.
588 Urgosik, Z. Starek, M. Crha, B. Blits, H. Petry, Z. Ellederova, J. Motlik, S. van Deventer, P.
589 Konstantinova, Widespread and sustained target engagement in Huntington's disease minipigs upon
590 intraatrial microRNA-based gene therapy. *Sci Transl Med* **13**, (2021).

591 8. L. Liu, M. E. Prime, M. R. Lee, V. Khetarpal, C. J. Brown, P. D. Johnson, P. Miranda-Azpiazu, X. Chen,
592 D. Clark-Frew, S. Coe, R. Davis, A. Dickie, A. Ebneith, S. Esposito, E. Gadouleau, X. Gai, S. Galan, S.
593 Green, C. Greenaway, P. Giles, C. Halldin, S. Hayes, T. Herbst, F. Herrmann, M. Hessmann, Z. Jia, A.
594 Kiselyov, A. Kotey, T. Krulle, J. E. Manette, R. W. Marston, S. Menta, M. R. Mills, E. Monteagudo, S.
595 Nag, M. Nibbio, L. Orsatti, S. Schaertl, C. Scheich, J. Sproston, V. Stepanov, M. Svedberg, A. Takano, M.
596 Taylor, W. Thomas, M. Toth, D. Vaidya, K. Vanras, D. Weddell, I. Wigginton, J. Wityak, L. Mrzljak, I.
597 Munoz-Sanjuan, J. A. Bard, C. Dominguez, Imaging Mutant Huntingtin Aggregates: Development of a
598 Potential PET Ligand. *J Med Chem* **63**, 8608-8633 (2020).

599 9. F. Herrmann, M. Hessmann, S. Schaertl, K. Berg-Rosseburg, C. J. Brown, G. Bursow, A. Chiki, A. Ebneith,
600 M. Gehrmann, N. Hoeschen, M. Hotze, S. Jahn, P. D. Johnson, V. Khetarpal, A. Kiselyov, K. Kottig, S.
601 Ladewig, H. Lashuel, S. Letschert, M. R. Mills, K. Petersen, M. E. Prime, C. Scheich, G. Schmiedel, J.
602 Wityak, L. Liu, C. Dominguez, I. Munoz-Sanjuan, J. A. Bard, Pharmacological characterization of mutant
603 huntingtin aggregate-directed PET imaging tracer candidates. *Sci Rep* **11**, 17977 (2021).

604 10. D. Bertoglio, J. Verhaeghe, A. Miranda, L. Wyffels, S. Stroobants, L. Mrzljak, V. Khetarpal, M. Skinbjerg,
605 L. Liu, C. Dominguez, I. Munoz-Sanjuan, J. Bard, S. Staelens, Longitudinal preclinical evaluation of the
606 novel radioligand [11C]CHDI-626 for PET imaging of mutant huntingtin aggregates in Huntington's
607 disease. *Eur J Nucl Med Mol Imaging*, (2021).

608 11. S. J. Tabrizi, M. D. Flower, C. A. Ross, E. J. Wild, Huntington disease: new insights into molecular
609 pathogenesis and therapeutic opportunities. *Nat Rev Neurol* **16**, 529-546 (2020).

610 12. B. Zeitler, S. Froelich, K. Marlen, D. A. Shivak, Q. Yu, D. Li, J. R. Pearl, J. C. Miller, L. Zhang, D. E.
611 Paschon, S. J. Hinkley, I. Ankoudinova, S. Lam, D. Guschin, L. Kopan, J. M. Cherone, H. B. Nguyen, G.
612 Qiao, Y. Ataei, M. C. Mendel, R. Amora, R. Surosky, J. Laganiere, B. J. Vu, A. Narayanan, Y. Sedaghat,
613 K. Tillack, C. Thiede, A. Gartner, S. Kwak, J. Bard, L. Mrzljak, L. Park, T. Heikkinen, K. K. Lehtimaki,
614 M. M. Svedberg, J. Haggkvist, L. Tari, M. Toth, A. Varrone, C. Halldin, A. E. Kudwa, S. Ramboz, M. Day,
615 J. Kondapalli, D. J. Surmeier, F. D. Urnov, P. D. Gregory, E. J. Rebar, I. Munoz-Sanjuan, H. S. Zhang,
616 Allele-selective transcriptional repression of mutant HTT for the treatment of Huntington's disease. *Nat*
617 *Med* **25**, 1131-1142 (2019).

- 618 13. T. Heikkinen, K. Lehtimäki, N. Vartiainen, J. Puolivali, S. J. Hendricks, J. R. Glaser, A. Bradaia, K. Wadel,
619 C. Touller, O. Kontkanen, J. M. Yrjänheikki, B. Buisson, D. Howland, V. Beaumont, I. Muñoz-Sanjuan, L.
620 C. Park, Characterization of neurophysiological and behavioral changes, MRI brain volumetry and 1H
621 MRS in zQ175 knock-in mouse model of Huntington's disease. *PLoS One* **7**, e50717 (2012).
- 622 14. L. B. Menalled, A. E. Kudwa, S. Miller, J. Fitzpatrick, J. Watson-Johnson, N. Keating, M. Ruiz, R.
623 Mushlin, W. Alosio, K. McConnell, D. Connor, C. Murphy, S. Oakeshott, M. Kwan, J. Beltran, A.
624 Ghavami, D. Brunner, L. C. Park, S. Ramboz, D. Howland, Comprehensive behavioral and molecular
625 characterization of a new knock-in mouse model of Huntington's disease: zQ175. *PLoS One* **7**, e49838
626 (2012).
- 627 15. D. S. Russell, D. L. Jennings, O. Barret, G. D. Tamagnan, V. M. Carroll, F. Caille, D. Alagille, T. J.
628 Morley, C. Papin, J. P. Seibyl, K. L. Marek, Change in PDE10 across early Huntington disease assessed by
629 [18F]MNI-659 and PET imaging. *Neurology* **86**, 748-754 (2016).
- 630 16. V. Beaumont, S. Zhong, H. Lin, W. Xu, A. Bradaia, E. Steidl, M. Gleyzes, K. Wadel, B. Buisson, F. E.
631 Padovan-Neto, S. Chakroborty, K. M. Ward, J. F. Harms, J. Beltran, M. Kwan, A. Ghavami, J. Haggkvist,
632 M. Toth, C. Halldin, A. Varrone, C. Schaab, J. N. Dybowski, S. Elschenbroich, K. Lehtimäki, T.
633 Heikkinen, L. Park, J. Rosinski, L. Mrzljak, D. Lavery, A. R. West, C. J. Schmidt, M. M. Zaleska, I.
634 Muñoz-Sanjuan, Phosphodiesterase 10A Inhibition Improves Cortico-Basal Ganglia Function in
635 Huntington's Disease Models. *Neuron* **92**, 1220-1237 (2016).
- 636 17. P. Fazio, C. J. Fitzer-Attas, L. Mrzljak, J. Bronzova, S. Nag, J. H. Warner, B. Landwehrmeyer, N. Al-
637 Tawil, C. Halldin, A. Forsberg, J. Ware, V. Dilda, A. Wood, C. Sampaio, A. Varrone, H. D. Pearl, L. s.
638 collaborators, PET Molecular Imaging of Phosphodiesterase 10A: An Early Biomarker of Huntington's
639 Disease Progression. *Mov Disord* **35**, 606-615 (2020).
- 640 18. R. A. Weeks, P. Piccini, A. E. Harding, D. J. Brooks, Striatal D1 and D2 dopamine receptor loss in
641 asymptomatic mutation carriers of Huntington's disease. *Ann Neurol* **40**, 49-54 (1996).
- 642 19. A. Antonini, K. L. Leenders, D. Eidelberg, [11C]raclopride-PET studies of the Huntington's disease rate of
643 progression: relevance of the trinucleotide repeat length. *Ann Neurol* **43**, 253-255 (1998).
- 644 20. N. Carty, N. Berson, K. Tillack, C. Thiede, D. Scholz, K. Kottig, Y. Sedaghat, C. Gabrysiak, G. Yohrling,
645 H. von der Kammer, A. Ebner, V. Mack, I. Muñoz-Sanjuan, S. Kwak, Characterization of HTT inclusion
646 size, location, and timing in the zQ175 mouse model of Huntington's disease: an in vivo high-content
647 imaging study. *PLoS One* **10**, e0123527 (2015).
- 648 21. P. Langfelder, J. P. Cattle, D. Chatzopoulou, N. Wang, F. Gao, I. Al-Ramahi, X. H. Lu, E. M. Ramos, K.
649 El-Zein, Y. Zhao, S. Deverasetty, A. Tebbe, C. Schaab, D. J. Lavery, D. Howland, S. Kwak, J. Botas, J. S.
650 Aaronson, J. Rosinski, G. Coppola, S. Horvath, X. W. Yang, Integrated genomics and proteomics define
651 huntingtin CAG length-dependent networks in mice. *Nat Neurosci* **19**, 623-633 (2016).
- 652 22. C. A. Gutekunst, S. H. Li, H. Yi, J. S. Mulroy, S. Kuemmerle, R. Jones, D. Rye, R. J. Ferrante, S. M.
653 Hersch, X. J. Li, Nuclear and neuropil aggregates in Huntington's disease: relationship to neuropathology. *J*
654 *Neurosci* **19**, 2522-2534 (1999).
- 655 23. J. Ko, J. M. Isas, A. Sabbaugh, J. H. Yoo, N. K. Pandey, A. Chongtham, M. Ladinsky, W. L. Wu, H.
656 Rohweder, A. Weiss, D. Macdonald, I. Muñoz-Sanjuan, R. Langen, P. H. Patterson, A. Khoshnan,
657 Identification of distinct conformations associated with monomers and fibril assemblies of mutant
658 huntingtin. *Hum Mol Genet* **27**, 2330-2343 (2018).
- 659 24. J. Verhaeghe, D. Bertoglio, L. Kosten, D. Thoma, M. Verhoye, A. Van Der Linden, L. Wyffels, S.
660 Stroobants, J. Wityak, C. Dominguez, L. Mrzljak, S. Staelens, Noninvasive Relative Quantification of
661 [(11C)ABP688 PET Imaging in Mice Versus an Input Function Measured Over an Arteriovenous Shunt.
662 *Front Neurol* **9**, 516 (2018).
- 663 25. D. Bertoglio, J. Verhaeghe, S. Korat, A. Miranda, L. Wyffels, S. Stroobants, L. Mrzljak, C. Dominguez, L.
664 Liu, M. Skinbjerg, I. Muñoz-Sanjuan, S. Staelens, In vitro and In vivo Assessment of Suitable Reference
665 Region and Kinetic Modelling for the mGluR1 Radioligand [(11C)ITDM in Mice. *Mol Imaging Biol*,
666 (2019).
- 667 26. R. B. Innis, V. J. Cunningham, J. Delforge, M. Fujita, A. Gjedde, R. N. Gunn, J. Holden, S. Houle, S. C.
668 Huang, M. Ichise, H. Iida, H. Ito, Y. Kimura, R. A. Koeppe, G. M. Knudsen, J. Knuuti, A. A. Lammertsma,
669 M. Laruelle, J. Logan, R. P. Maguire, M. A. Mintun, E. D. Morris, R. Parsey, J. C. Price, M. Slifstein, V.
670 Sossi, T. Suhara, J. R. Votaw, D. F. Wong, R. E. Carson, Consensus nomenclature for in vivo imaging of
671 reversibly binding radioligands. *J Cereb Blood Flow Metab* **27**, 1533-1539 (2007).
- 672 27. J. Logan, J. S. Fowler, N. D. Volkow, A. P. Wolf, S. L. Dewey, D. J. Schlyer, R. R. MacGregor, R.
673 Hitzemann, B. Bendriem, S. J. Gatley, et al., Graphical analysis of reversible radioligand binding from

- 674 time-activity measurements applied to [N-11C-methyl]-(-)-cocaine PET studies in human subjects. *J Cereb*
675 *Blood Flow Metab* **10**, 740-747 (1990).
- 676 28. B. Dehay, C. Weber, Y. Trottier, A. Bertolotti, Mapping of the epitope of monoclonal antibody 2B4 to the
677 proline-rich region of human Huntingtin, a region critical for aggregation and toxicity. *Biotechnol J* **2**, 559-
678 564 (2007).
- 679 29. G. Sciacca, F. Cicchetti, Mutant huntingtin protein expression and blood-spinal cord barrier dysfunction in
680 huntington disease. *Ann Neurol* **82**, 981-994 (2017).
- 681 30. N. Pavese, M. Politis, Y. F. Tai, R. A. Barker, S. J. Tabrizi, S. L. Mason, D. J. Brooks, P. Piccini, Cortical
682 dopamine dysfunction in symptomatic and premanifest Huntington's disease gene carriers. *Neurobiol Dis*
683 **37**, 356-361 (2010).
- 684 31. T. C. Andrews, R. A. Weeks, N. Turjanski, R. N. Gunn, L. H. Watkins, B. Sahakian, J. R. Hodges, A. E.
685 Rosser, N. W. Wood, D. J. Brooks, Huntington's disease progression. PET and clinical observations. *Brain*
686 **122** (Pt 12), 2353-2363 (1999).
- 687 32. C. C. Tang, A. Feigin, Y. Ma, C. Habeck, J. S. Paulsen, K. L. Leenders, L. K. Teune, J. C. van Oostrom,
688 M. Guttman, V. Dhawan, D. Eidelberg, Metabolic network as a progression biomarker of premanifest
689 Huntington's disease. *J Clin Invest* **123**, 4076-4088 (2013).
- 690 33. J. Haggkvist, M. Toth, L. Tari, K. Varnas, M. Svedberg, A. Forsberg, S. Nag, C. Dominguez, I. Munoz-
691 Sanjuan, J. Bard, J. Wityak, A. Varrone, C. Halldin, L. Mrzljak, Longitudinal Small-Animal PET Imaging
692 of the zQ175 Mouse Model of Huntington Disease Shows In Vivo Changes of Molecular Targets in the
693 Striatum and Cerebral Cortex. *J Nucl Med* **58**, 617-622 (2017).
- 694 34. D. Bertoglio, J. Verhaeghe, L. Kosten, D. Thomae, A. Van der Linden, S. Stroobants, J. Wityak, C.
695 Dominguez, L. Mrzljak, S. Staelens, MR-based spatial normalization improves [18F]MNI-659 PET
696 regional quantification and detectability of disease effect in the Q175 mouse model of Huntington's disease.
697 *PLoS One* **13**, e0206613 (2018).
- 698 35. D. Bertoglio, J. Verhaeghe, A. Miranda, L. Wyffels, S. Stroobants, C. Dominguez, I. Munoz-Sanjuan, M.
699 Skinbjerg, L. Liu, S. Staelens, Kinetic Modelling and Test-Retest Reproducibility for the Dopamine D1R
700 Radioligand [(11)C]SCH23390 in Healthy and Diseased Mice. *Mol Imaging Biol* **23**, 208-219 (2021).
- 701 36. D. Macdonald, M. A. Tessari, I. Boogaard, M. Smith, K. Pulli, A. Szynol, F. Albertus, M. B. Lamers, S.
702 Dijkstra, D. Kordt, W. Reindl, F. Herrmann, G. McAllister, D. F. Fischer, I. Munoz-Sanjuan,
703 Quantification assays for total and polyglutamine-expanded huntingtin proteins. *PLoS One* **9**, e96854
704 (2014).
- 705 37. W. Reindl, B. Baldo, J. Schulz, I. Janack, I. Lindner, M. Kleinschmidt, Y. Sedaghat, C. Thiede, K. Tillack,
706 C. Schmidt, I. Cardaun, T. Schwagarus, F. Herrmann, M. Hotze, G. F. Osborne, S. Herrmann, A. Weiss, C.
707 Zerbinatti, G. P. Bates, J. Bard, I. Munoz-Sanjuan, D. Macdonald, Meso scale discovery-based assays for
708 the detection of aggregated huntingtin. *PLoS One* **14**, e0213521 (2019).
- 709 38. E. A. Spronck, C. C. Brouwers, A. Valles, M. de Haan, H. Petry, S. J. van Deventer, P. Konstantinova, M.
710 M. Evers, AAV5-miHTT Gene Therapy Demonstrates Sustained Huntingtin Lowering and Functional
711 Improvement in Huntington Disease Mouse Models. *Mol Ther Methods Clin Dev* **13**, 334-343 (2019).
- 712 39. N. S. Caron, A. L. Southwell, C. C. Brouwers, L. D. Cengio, Y. Xie, H. F. Black, L. M. Anderson, S. Ko,
713 X. Zhu, S. J. van Deventer, M. M. Evers, P. Konstantinova, M. R. Hayden, Potent and sustained huntingtin
714 lowering via AAV5 encoding miRNA preserves striatal volume and cognitive function in a humanized
715 mouse model of Huntington disease. *Nucleic Acids Res* **48**, 36-54 (2020).
- 716 40. L. B. Menalled, J. D. Sison, I. Dragatsis, S. Zeitlin, M. F. Chesselet, Time course of early motor and
717 neuropathological anomalies in a knock-in mouse model of Huntington's disease with 140 CAG repeats. *J*
718 *Comp Neurol* **465**, 11-26 (2003).
- 719 41. D. Bertoglio, J. Verhaeghe, S. Korat, A. Miranda, L. Wyffels, S. Stroobants, L. Mrzljak, C. Dominguez, L.
720 Liu, M. Skinbjerg, I. Munoz-Sanjuan, S. Staelens, In vitro and In vivo Assessment of Suitable Reference
721 Region and Kinetic Modelling for the mGluR1 Radioligand [(11)C]ITDM in Mice. *Mol Imaging Biol* **22**,
722 854-863 (2020).
- 723 42. P. Zanotti-Fregonara, K. Chen, J. S. Liow, M. Fujita, R. B. Innis, Image-derived input function for brain
724 PET studies: many challenges and few opportunities. *J Cereb Blood Flow Metab* **31**, 1986-1998 (2011).
- 725 43. D. Bertoglio, J. Verhaeghe, L. Wyffels, A. Miranda, S. Stroobants, L. Mrzljak, C. Dominguez, M.
726 Skinbjerg, J. Bard, L. Liu, I. Munoz-Sanjuan, S. Staelens, Synaptic vesicle glycoprotein 2A is affected in
727 the CNS of Huntington's Disease mice and post-mortem human HD brain. *J Nucl Med*, (In press).
- 728 44. D. Bertoglio, J. Verhaeghe, S. Korat, A. Miranda, K. Cybulska, L. Wyffels, S. Stroobants, L. Mrzljak, C.
729 Dominguez, M. Skinbjerg, L. Liu, I. Munoz-Sanjuan, S. Staelens, Elevated Type 1 Metabotropic Glutamate

- 730 Receptor Availability in a Mouse Model of Huntington's Disease: a Longitudinal PET Study. *Mol*
731 *Neurobiol.*, (2020).
- 732 45. D. Bertoglio, J. Verhaeghe, A. Miranda, I. Kertesz, K. Cybulska, S. Korat, L. Wyffels, S. Stroobants, L.
733 Mrzljak, C. Dominguez, L. Liu, M. Skinbjerg, I. Munoz-Sanjuan, S. Staelens, Validation and noninvasive
734 kinetic modeling of [(11)C]UCB-J PET imaging in mice. *J Cereb Blood Flow Metab* **40**, 1351-1362
735 (2020).
- 736 46. D. Bertoglio, L. Kosten, J. Verhaeghe, D. Thomae, L. Wyffels, S. Stroobants, J. Wityak, C. Dominguez, L.
737 Mrzljak, S. Staelens, Longitudinal characterization of mGluR5 using (11)C-ABP688 PET imaging in the
738 Q175 mouse model of Huntington's disease. *J Nucl Med.*, (2018).
- 739 47. D. Bertoglio, J. Verhaeghe, A. Miranda, L. Wyffels, S. Stroobants, C. Dominguez, I. Munoz-Sanjuan, M.
740 Skinbjerg, L. Liu, S. Staelens, Kinetic Modelling and Test-Retest Reproducibility for the Dopamine D1R
741 Radioligand [(11)C]SCH23390 in Healthy and Diseased Mice. *Mol Imaging Biol.*, (2020).
- 742 48. A. Miranda, S. Staelens, S. Stroobants, J. Verhaeghe, Motion dependent and spatially variant resolution
743 modeling for PET rigid motion correction. *IEEE Trans Med Imaging.*, (2020).
- 744 49. G. A. Johnson, A. Badea, J. Brandenburg, G. Cofer, B. Fubara, S. Liu, J. Nissanov, Waxholm space: an
745 image-based reference for coordinating mouse brain research. *Neuroimage* **53**, 365-372 (2010).
- 746 50. R. N. Gunn, A. A. Lammertsma, S. P. Hume, V. J. Cunningham, Parametric imaging of ligand-receptor
747 binding in PET using a simplified reference region model. *Neuroimage* **6**, 279-287 (1997).
- 748 51. Y. J. Wu, R. E. Carson, Noise reduction in the simplified reference tissue model for neuroreceptor
749 functional Imaging. *J Cerebr Blood F Met* **22**, 1440-1452 (2002).
- 750 52. Z. Bayram-Weston, L. Jones, S. B. Dunnett, S. P. Brooks, Comparison of mHTT Antibodies in
751 Huntington's Disease Mouse Models Reveal Specific Binding Profiles and Steady-State Ubiquitin Levels
752 with Disease Development. *PLoS One* **11**, e0155834 (2016).
- 753 53. M. Minderer, W. Liu, L. T. Sumanovski, S. Kugler, F. Helmchen, D. J. Margolis, Chronic imaging of
754 cortical sensory map dynamics using a genetically encoded calcium indicator. *J Physiol* **590**, 99-107
755 (2012).
- 756 54. C. Halldin, S. Stone-Elander, L. Farde, E. Ehrin, K. J. Fasth, B. Langstrom, G. Sedvall, Preparation of 11C-
757 labelled SCH 23390 for the in vivo study of dopamine D-1 receptors using positron emission tomography.
758 *Int J Rad Appl Instrum A* **37**, 1039-1043 (1986).
- 759 55. E. Ehrin, L. Farde, T. de Paulis, L. Eriksson, T. Greitz, P. Johnstrom, J. E. Litton, J. L. Nilsson, G. Sedvall,
760 S. Stone-Elander, et al., Preparation of 11C-labelled Raclopride, a new potent dopamine receptor
761 antagonist: preliminary PET studies of cerebral dopamine receptors in the monkey. *Int J Appl Radiat Isot*
762 **36**, 269-273 (1985).
- 763 56. G. Paxinos, K. Franklin, *The mouse brain in stereotaxic coordinates.* (Academic Press; 2 edition
764 (December 8, 2003), 2003), pp. 350.
765

766

767 **Acknowledgments**

768 The authors thank Philippe Joye, Caroline Berghmans, Eleni Van der Hallen, Romy Raeymakers,
769 Silvia Incardona, and Annemie Van Eetveldt of the Molecular Imaging Center Antwerp (MICA),
770 Stefanie Jahn, Nicole Hoeschen, Aglaia Kakoulidou, Isabell Cardaun, Antje Cornelius, Christina
771 Schmidt, and Tom Schwagarus at Evotec Hamburg for their important and valuable technical
772 support, Evelyn Galstian, Maya Bader, and Brenda Lager for project and animal management
773 support and administration, as well as Dr. Simon Noble for help with proofreading the manuscript.
774 DB is supported by a post-doctoral fellowship from the Research Foundation Flanders (FWO,
775 1229721N). Antwerp University, Belgium supported the work through a partial assistant professor
776 position to JV and a full professor position to SSt. DB, AVdL, JV, and SSt are members of the

777 μ Neuro Research Centre of Excellence at the University of Antwerp. Timelines of Figures 2, 3, 4,
778 5, S3, and S10 were generated using BioRender.

779

780

781 **Author contributions**

782 Conception and design of the studies: DB, JB, LL, MH, AG, CD, JV, SSt and IM-S

783 In vitro assays and studies: DB, MH, FP, FH, and SSc

784 Chemistry design of ligands and synthetic routes: CB, PJ, MP, and MM

785 Injection ZFP for studies: AG and BH

786 MRI: DB, TV, and AVdL

787 Synthesis of radioligands: SDL

788 In vivo PET studies: DB, AM, FZ, JV, and SSt

789 Post-mortem studies: DB, MH, and FZ

790 Supervised the experiments: DB, JB, LL, MH, AG, LM, VK, YW, DM, MS, JV, CD, SSt, and IM-

791 S

792 Interpretation of the results: DB, JB, MH, LL, AG, LM, VK, YW, DM, MS, JV, CD, SSt, and IM-

793 S

794 Prepared final Figures: DB

795 Writing – original draft: DB, JB, MH, AG, and IM-S

796

797 **Competing interests**

798 This work was supported by the non-profit CHDI Foundation, Inc. JB, LL, LM, VK, YW, DM,

799 MS, CD, IM-S are employed by CHDI Management, Inc. as advisors to CHDI Foundation, Inc.,

800 and declare no conflict of interest. CHDI Foundation, Inc. is a nonprofit biomedical research

801 organization exclusively dedicated to developing therapeutics that substantially improve the lives

802 of those affected by Huntington's disease, and conducts research in a number of different ways.

803 The following granted patent is related to this work: Probes for Imaging Huntingtin Proteins,

804 International Publication Number WO 2016/033445 A1 (published on 3 March 2016 with filing

805 number #PCT/US20 15/047407).

806

807

808 **Data availability**

809 All data associated with this study are presented in the paper or the Supplementary Materials. Any
810 request for material reported in this study will be available through a material transfer agreement
811 (MTA) between requestor and CHDI Foundation, Inc..

812

813

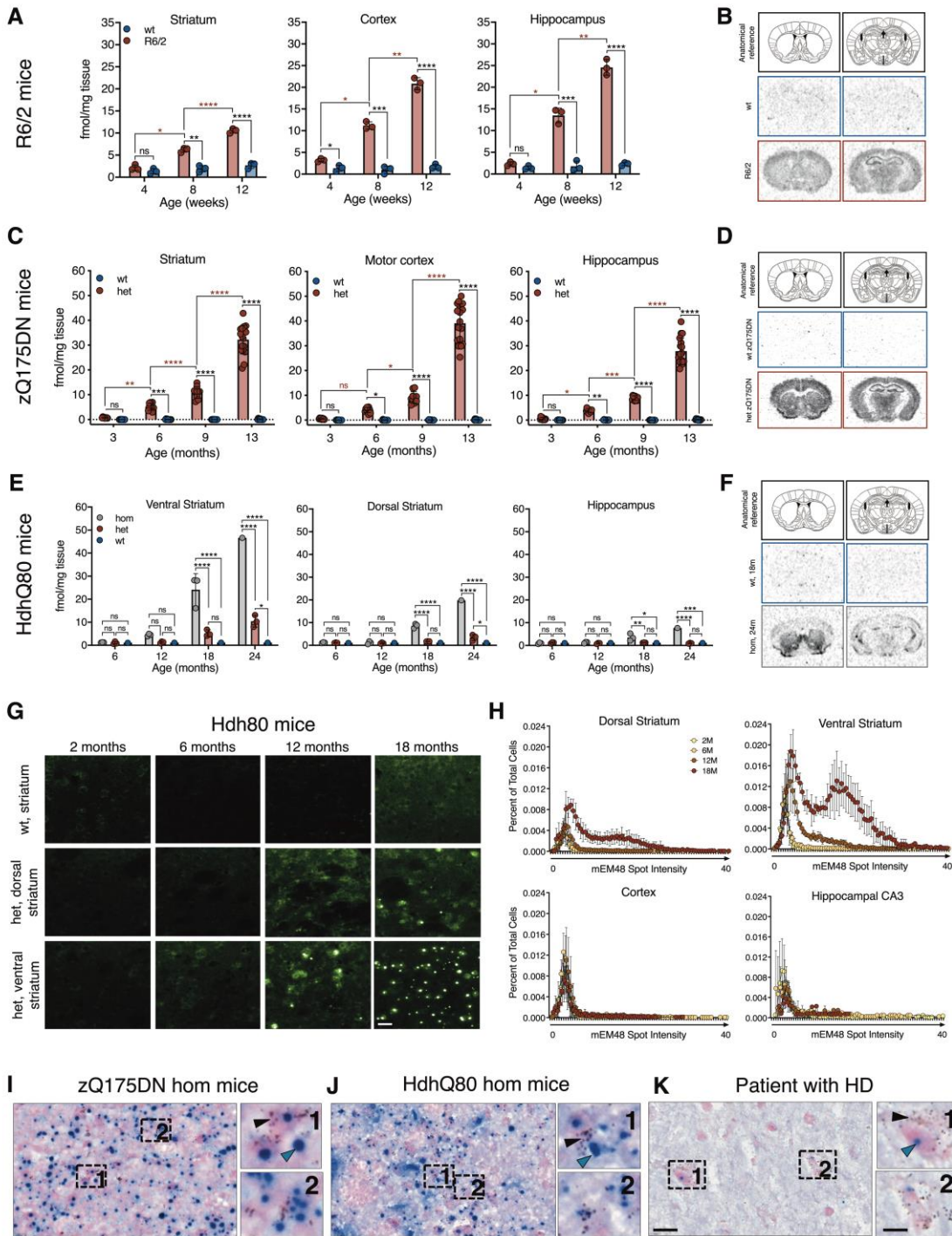
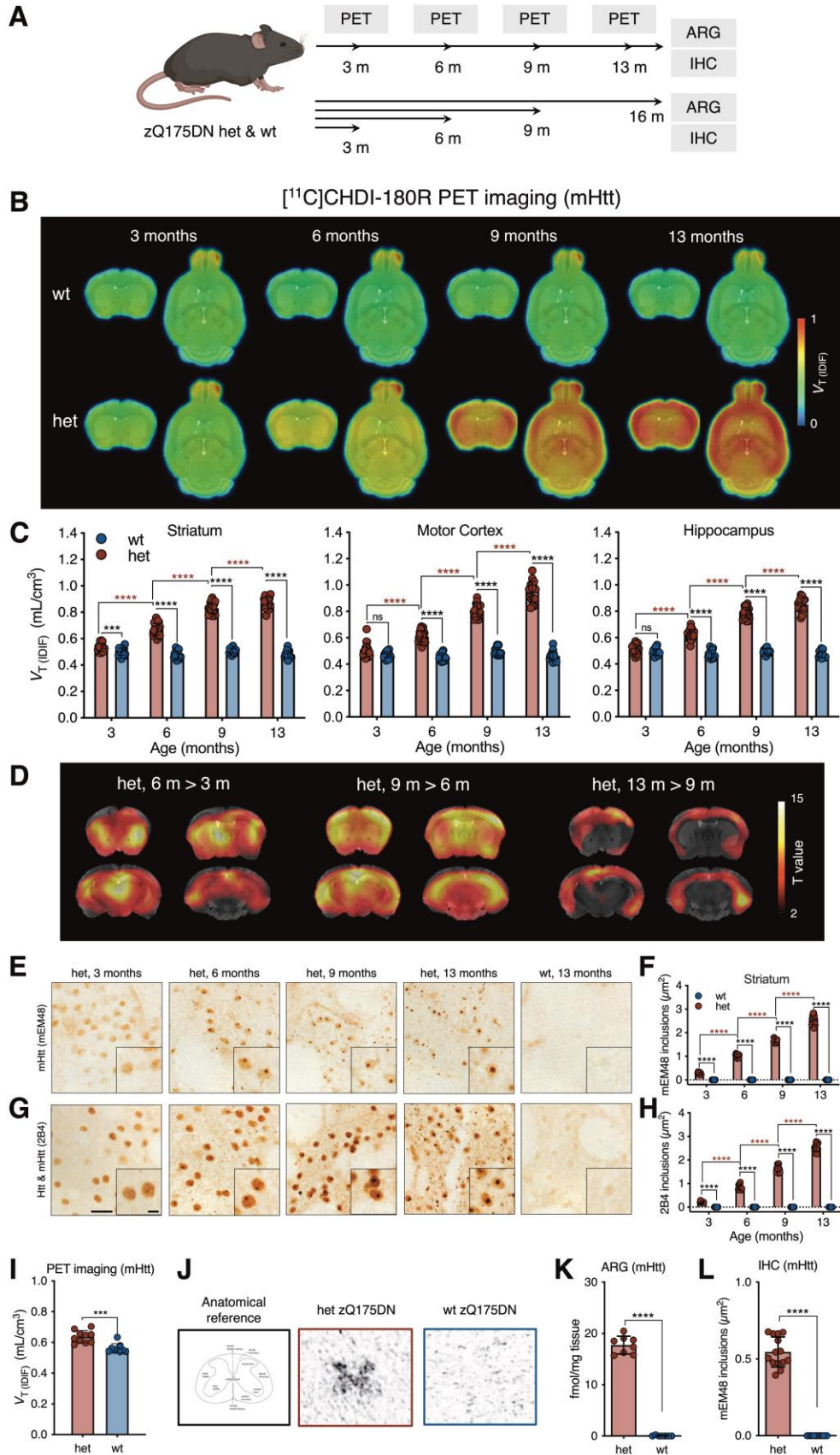


Fig. 1.

815

816 **[³H]CHDI-180 mHTT-specific binding in HD mouse models without colocalizing with**
 817 **mHTT inclusions. (A,B),** Binding to transgenic R6/2 CAG120 mouse brains expressing mutant
 818 human exon1 Htt. (A) Genotype-specific age-dependent increase in [³H]CHDI-180 in striatum,
 819 cortex, and hippocampus of 4-, 8-, and 12-week-old R6/2 CAG120 and wt littermates (wt, *n*=3;

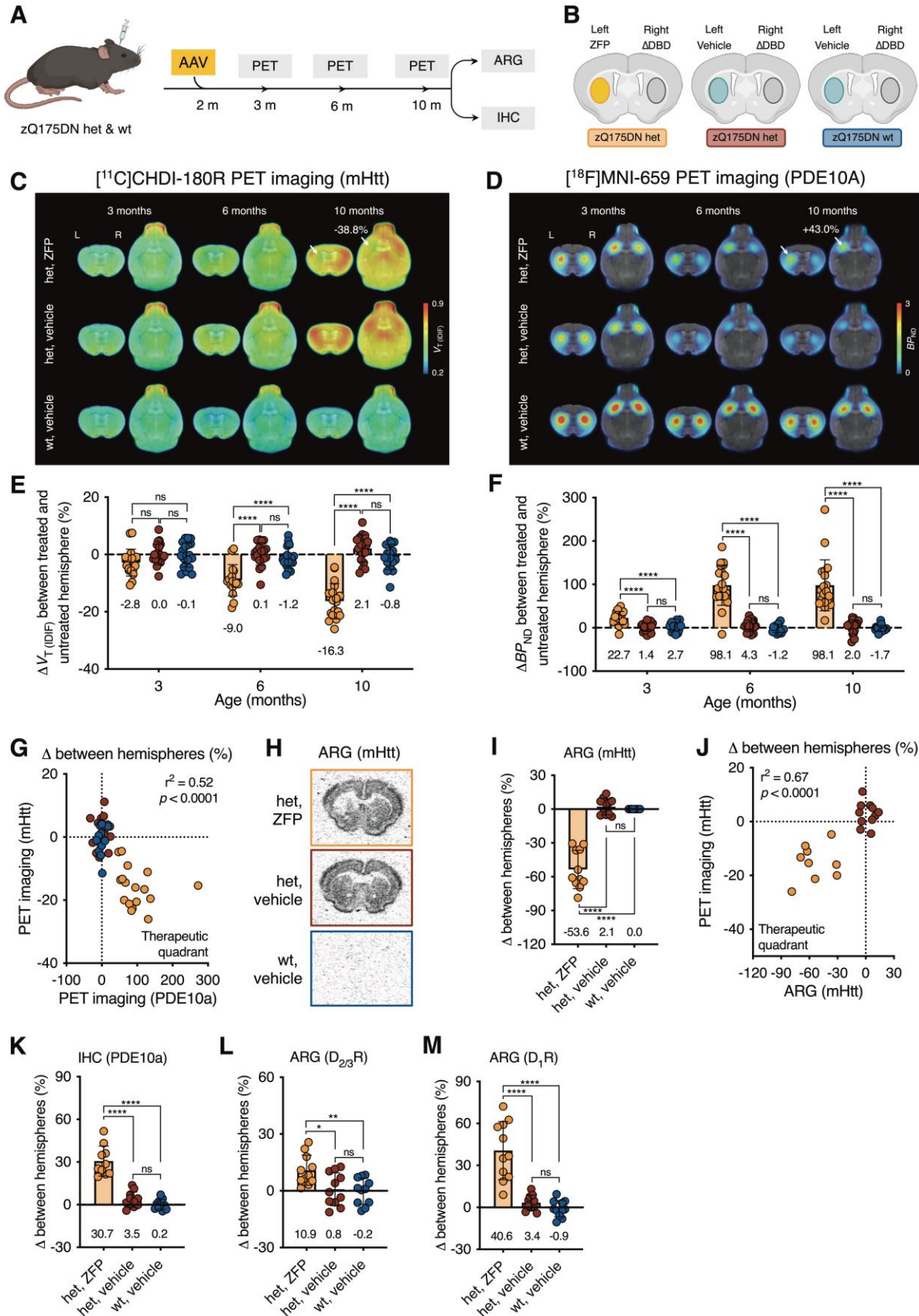
820 R6/2, $n=3$; per age). Two-way ANOVA with Tukey's multiple comparison test. Red asterisk
821 denotes signal differences between ages, as indicated for R6/2 mice. One representative study
822 out of $n>15$ experiments shown. **(B)** Representative autoradiograms showing total binding of
823 [^3H]CHDI-180 in the striatum, cortex, and hippocampus of 12-week-old R6/2 and wt mice;
824 anatomical orientation as indicated. **(C,D)** Binding to knock-in zQ175DN het mouse brains
825 carrying a humanized exon1 Htt sequence with 198 CAG repeats. **c**, Genotype-specific age-
826 dependent increase in [^3H]CHDI-180 in striatum, cortex, and hippocampus of 3, 6, 9 months (wt,
827 $n=10$; het, $n=10$, per age), and 13 months (wt, $n=13$; het, $n=17$) of age. Two-way ANOVA with
828 Tukey's multiple comparison test. Red asterisk denotes signal differences between ages, as
829 indicated for zQ175DN het mice. **(D)** Representative autoradiograms showing total binding of
830 [^3H]CHDI-180 in striatum, cortex, and hippocampus of 13-month-old zQ175DN het and wt
831 mice; anatomical orientation as indicated. **(E-H)** Binding to knock-in HdhQ80 mouse brains
832 carrying a humanized exon1 Htt sequence with 86 CAG repeats. **(E)** Genotype-specific age-
833 dependent increase in [^3H]CHDI-180 in ventral and dorsal striatum as well as hippocampus at 6,
834 9, 18, and 24 months (wt, $n=1-3$; het, $n=3$; hom, $n=1-3$, per age) of age. Two-way ANOVA with
835 Tukey's multiple comparison test. **(F)** Representative autoradiograms showing total binding of
836 [^3H]CHDI-180 in striatum, cortex, and hippocampus of 24-month-old HdhQ80 hom and wt
837 mice; anatomical orientation as indicated. **(G)** Representative mHTT inclusions (mEM48)
838 immunostaining in the dorsal and ventral striatum of HdhQ80 wt and het mice indicates that
839 [^3H]CHDI-180 binding is associated with the age- and brain region-dependent appearance of
840 mEM48-positive mHTT inclusions as shown by mEM48 immunohistochemistry Scale bar, 20
841 μm . **(H)** Quantitative analysis of mEM48 intensity in HdhQ80 mice for mHTT inclusions in
842 different brain regions and age groups. **(I-K)** Colocalization of [^3H]CHDI-180 binding and
843 mHTT inclusions (mEM48) in the ventral striatum of 12-month-old hom zQ175DN mice **(I)**,
844 ventral striatum of 24-month-old hom Hdh80 mice **(J)**, and post-mortem frontal cortex of a
845 patient with HD (#2017-060) **(K)**. [^3H]CHDI-180 silver grain signal was detectable in close
846 vicinity to mEM48-positive signal but never co-registered with mHTT inclusion bodies, although
847 it was partially co-registered with more diffuse appearing mEM48-positive signal. [^3H]CHDI-
848 180 binding, black silver grains, black arrowhead; mHTT inclusions (mEM48), blue, blue
849 arrowhead; background tissue (Nuclear Fast Red), pink. Scale bar, 20 μm ; inset, 10 μm . Data are
850 shown as mean \pm s.d., all points are shown; * $P<0.05$, ** $P<0.01$, *** $P<0.001$, **** $P<0.0001$.



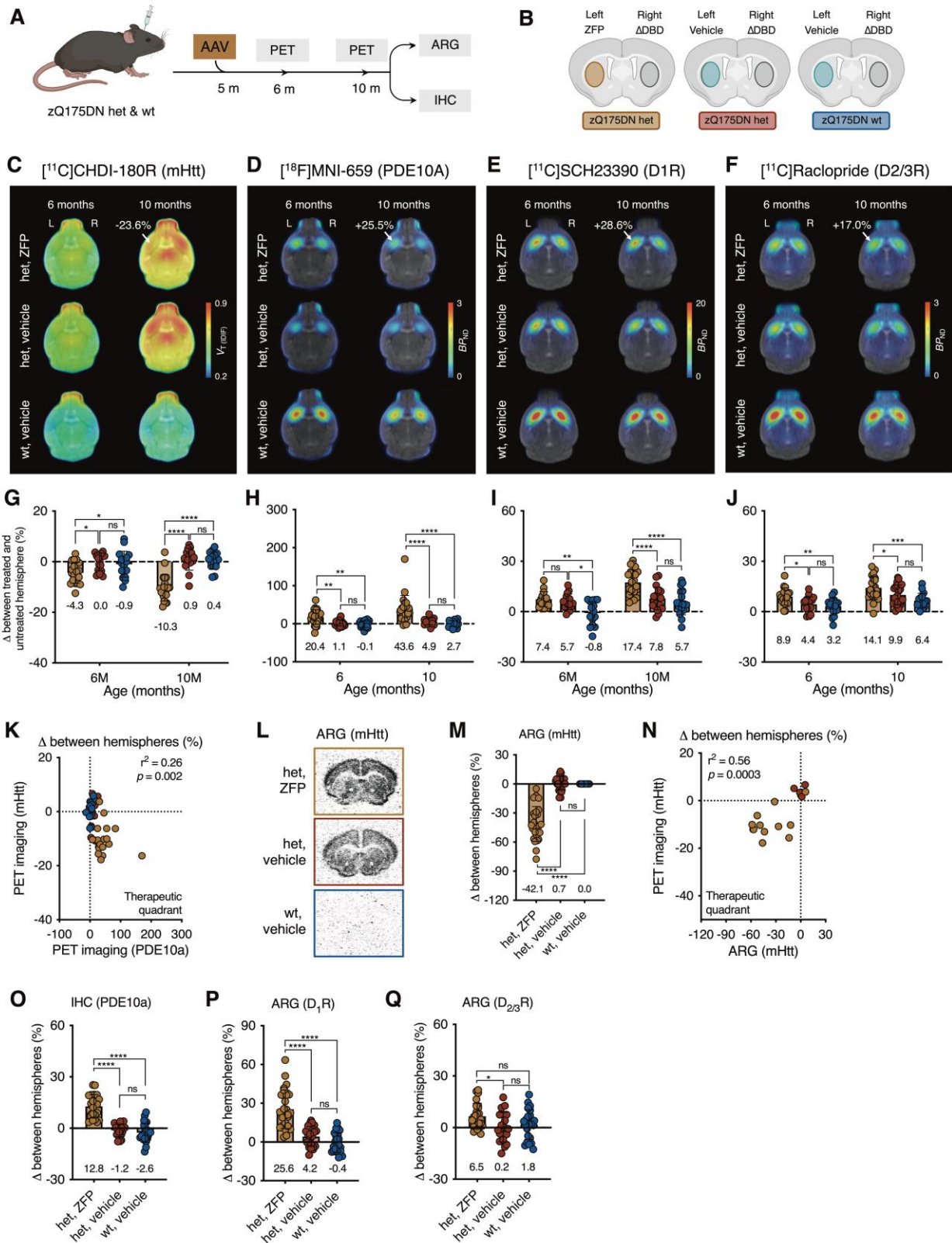
852 **Fig. 2. Longitudinal characterization of natural disease in zQ175DN het mice using**
853 **[¹¹C]CHDI-180R PET imaging.** (A) Timeline overview and endpoints in zQ175DN wt and het
854 mice. Upper timeline refers to the longitudinal in vivo study, whereas lower one to the cross-
855 sectional post-mortem studies. (B) Mean [¹¹C]CHDI-180R V_T (IDIF) parametric images of
856 zQ175DN wt and het mice at 3, 6, 9, and 13 months of age. PET images are co-registered to the
857 MRI template for anatomical reference. Coronal and axial planes are shown. (C) Regional
858 [¹¹C]CHDI-180R V_T (IDIF) quantification in zQ175DN wt and het at 3 months (wt, $n=19$; het, $n=21$),
859 6 months (wt, $n=15$; het, $n=23$), 9 months (wt, $n=13$; het, $n=20$), and 13 months (wt, $n=12$; het,
860 $n=17$) of age. Repeated measures with linear mixed model analysis with Tukey-Kramer correction;
861 $***P<0.001$, $****P<0.0001$. Red asterisks denote longitudinal differences within zQ175DN het
862 mice. (D) Within zQ175DN het voxel-based analysis of [¹¹C]CHDI-180R V_T (IDIF) parametric
863 images. Comparison between 3-6 months ($n=21$), 6-9 months ($n=20$), and 9-13 months ($n=17$) of
864 age. Significant ($P<0.001$) clusters are co-registered to the MRI template for anatomical reference
865 and shown in the coronal panel. (E,G) Genotype-specific age-dependent accumulation of mHTT
866 inclusions in zQ175DN het mice at time points matching the longitudinal [¹¹C]CHDI-180R PET
867 study as demonstrated by mEM48 (e) and 2B4 (G) immunostaining. Scale bar, 20 μ m, inset scale
868 bar, 5 μ m. (F,H) Quantification of inclusions in wt and zQ175DN het mice for mEM48 (F) and
869 2B4 (H) at 3 months (wt, $n=10$; het, $n=10$), 6 months (wt, $n=10$; het, $n=10$), 9 months (wt, $n=10$;
870 het, $n=10$), and 13 months (wt, $n=13$; het, $n=17$) of age. Two-way ANOVA with Bonferroni's
871 multiple comparison test. Red asterisks denote longitudinal differences within zQ175DN het mice.
872 (I) Spinal cord [¹¹C]CHDI-180R V_T (IDIF) quantification in zQ175DN wt and het at 13 months (wt,
873 $n=9$; het, $n=10$) of age. Two-tailed unpaired t-test with Welch's correction. (J) Representative
874 autoradiograms showing total binding of [³H]CHDI-180 in the spinal cord of zQ175DN wt and het
875 mice at 16 months; anatomical reference as indicated. (K) Specific binding of [³H]CHDI-180 in
876 the spinal cord of zQ175DN wt and het mice at 16 months (wt, $n=7$; het, $n=8$) of age. Two-tailed
877 unpaired t-test with Welch's correction. (L) Quantification of spinal cord inclusions in zQ175DN
878 wt and het mice for mEM48 at 16 months (wt, $n=13$; het, $n=15$) of age. Two-tailed unpaired t-test
879 with Welch's correction; $****P<0.0001$. ARG=autoradiography. Data are shown as mean \pm s.d.,
880 all points shown; $***P<0.001$, $****P<0.0001$.

881

882



884 **Fig. 3. Response of [¹¹C]CHDI-180R and imaging markers to early ZFP intervention in the**
885 **striatum of zQ175DN mice. (A)** Timeline overview and endpoints of early ZFP intervention in
886 zQ175DN wt and het mice. **(B)** Experimental design overview in zQ175DN wt and het mice
887 depicting injection hemisphere for ZFP treatment, ZFP-ΔDBD, and vehicle only. Fill colors
888 represent the experimental group animals belong to. **(C,D)** Mean [¹¹C]CHDI-180R V_T (IDIF) (mHTT
889 inclusions) **(C)** and [¹⁸F]MNI-659 BP_{ND} (PDE10a) **(D)** parametric images of zQ175DN wt vehicle,
890 het vehicle, and het ZFP-treated mice at 3, 6, and 10 months of age. PET images are co-registered
891 to the MRI template for anatomical reference. Coronal and axial planes are shown. A white arrow
892 at 10 months of age indicates the ZFP-treated striatal hemisphere with reduced mHTT and
893 increased PDE10a binding. **(E,F)** Percentage contralateral difference for striatal [¹¹C]CHDI-180R
894 V_T (IDIF) (mHTT inclusions) **(E)** and [¹⁸F]MNI-659 BP_{ND} (PDE10a) **(F)** quantification in zQ175DN
895 wt vehicle, het vehicle, and het ZFP-treated mice at 3, 6, and 10 months of age (het ZFP, $n=18-21$;
896 het vehicle, $n=18-22$; wt vehicle, $n=18-20$; values for each age, group, and radioligand) following
897 striatal injection at 2 months of age. Repeated measures with linear mixed model analysis with
898 Tukey-Kramer correction. **(G)** Correlation between contralateral difference for striatal mHTT and
899 PDE10a binding with the het, ZFP group deviating from the center of axes towards the therapeutic
900 quadrant. Two-tailed Pearson correlation analysis; $R^2=0.52$; $P<0.0001$. **(H)** Representative
901 autoradiograms showing total binding of [³H]CHDI-180 (mHTT inclusions) in zQ175DN wt
902 vehicle, het vehicle, and het ZFP-treated mice. **(I)** Percentage contralateral difference for striatal
903 specific binding of [³H]CHDI-180 in zQ175DN wt vehicle, het vehicle, and het ZFP-treated mice
904 at 10 months of age (het ZFP, $n=11$; het vehicle, $n=11$; wt vehicle, $n=11$) following striatal
905 injection at 2 months of age. One-way ANOVA with Tukey's multiple comparison test. **(J)**
906 Correlation between contralateral difference for striatal mHTT binding measured with microPET
907 and autoradiography at 10 months of age depicting the het ZFP-treated mice deviating from the
908 center of axes towards the therapeutic quadrant. Two-tailed Pearson correlation analysis; $R^2=0.67$;
909 $P<0.0001$. **(K-M)** Percentage contralateral difference for PDE10a immunostaining **(K)**,
910 [³H]SCH23390 (D_{1R}) **(L)**, [³H]Raclopride ($D_{2/3R}$) **(M)** in zQ175DN wt vehicle, het vehicle, and
911 het ZFP-treated mice at 10 months of age (het ZFP, $n=11$; het vehicle, $n=11$; wt vehicle, $n=11$)
912 following striatal injection at 2 months of age. One-way ANOVA with Tukey's multiple
913 comparison test. ARG=autoradiography. Data are shown as mean \pm s.d., all points shown;
914 * $P<0.05$, ** $P<0.01$, *** $P<0.001$, **** $P<0.0001$.



915

916

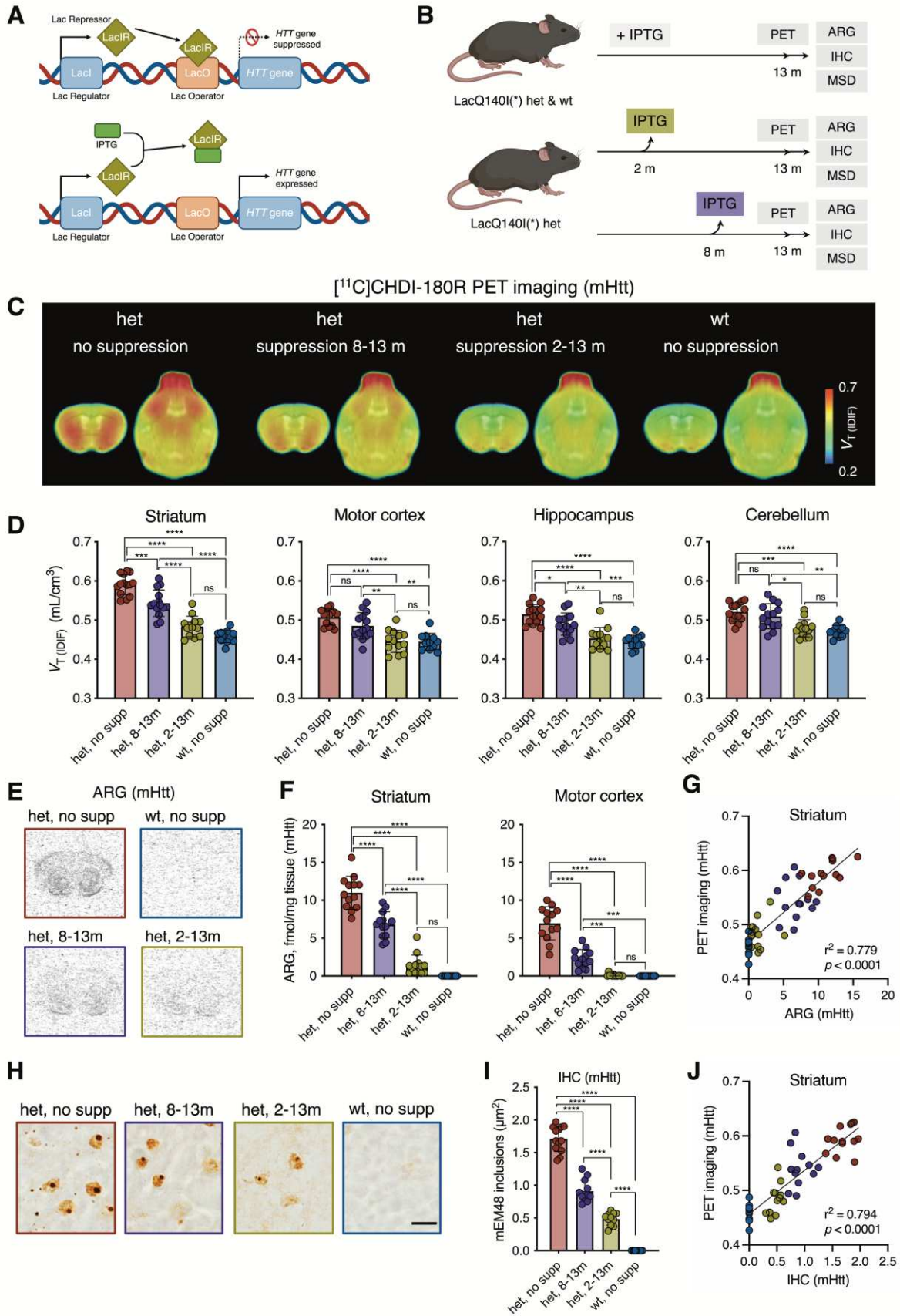
Fig. 4. Response of [¹¹C]CHDI-180R and imaging markers to late ZFP intervention in the

917 **striatum of zQ175DN mice.** (A) Timeline overview and endpoints of late ZFP intervention in
918 zQ175DN wt and het mice. (B) Experimental design overview in zQ175DN wt and het mice
919 depicting injection hemisphere for ZFP treatment, ZFP-ΔDBD, and vehicle only. Fill colors
920 represent the experimental group animals belong to. (C-F) Mean [¹¹C]CHDI-180R V_T (IDIF) (mHTT
921 inclusions) (C), [¹⁸F]MNI-659 BP_{ND} (PDE10a) (D), [¹¹C]SCH23390 BP_{ND} (D₁R) (E), and
922 [¹¹C]Raclopride BP_{ND} (D_{2/3}R) (F) parametric images of zQ175DN wt vehicle, het vehicle, and het
923 ZFP-treated mice at 6 and 10 months of age. PET images are co-registered to the MRI template
924 for anatomical reference. Axial plane is shown. A white arrow at 10 months of age indicates the
925 ZFP-treated striatal hemisphere with reduced mHTT as well as increased PDE10a, D₁R, and D_{2/3}R
926 binding. (G-J) Percentage contralateral difference for striatal [¹¹C]CHDI-180R V_T (IDIF) (mHTT
927 inclusions) (G), [¹⁸F]MNI-659 BP_{ND} (PDE10a) (H), [¹¹C]SCH23390 BP_{ND} (D₁R) (I), and
928 [¹¹C]Raclopride BP_{ND} (D_{2/3}R) (J) quantification in zQ175DN wt vehicle, het vehicle, and het ZFP-
929 treated mice at 6 and 10 months of age (het ZFP, $n=17-23$; het vehicle, $n=16-22$; wt vehicle, $n=16-22$;
930 19; values for each age, group, and radioligand) following striatal injection at 5 months of age.
931 Repeated measures with linear mixed model analysis with Tukey-Kramer correction. (K)
932 Correlation between contralateral difference for striatal mHTT and PDE10a binding with the het,
933 ZFP group partly deviating from the center of axes towards the therapeutic quadrant. Two-tailed
934 Pearson correlation analysis; $R^2=0.26$; $P=0.002$. (L) Representative autoradiograms showing total
935 binding of [³H]CHDI-180 (mHTT inclusions) in zQ175DN wt vehicle, het vehicle, and het ZFP-
936 treated. (M) Percentage contralateral difference for striatal specific binding of [³H]CHDI-180 in
937 zQ175DN wt vehicle, het vehicle, and het ZFP-treated mice at 10 months of age (het ZFP, $n=25$;
938 het vehicle, $n=26$; wt vehicle, $n=25$) following striatal injection at 5 months of age. One-way
939 ANOVA with Tukey's multiple comparison test. (N) Correlation between contralateral difference
940 for striatal mHTT binding measured with microPET and autoradiography at 10 months of age
941 depicting the het ZFP-treated mice partly deviating from the center of axes towards the therapeutic
942 quadrant. Two-tailed Pearson correlation analysis; $R^2=0.56$; $P=0.0003$. (O-Q) Percentage
943 contralateral difference for immunostaining for PDE10a (O), and autoradiography for
944 [³H]SCH23390 (D₁R) (P), [³H]Raclopride (D_{2/3}R) (Q) in zQ175DN wt vehicle, het vehicle, and
945 het ZFP-treated mice at 10 months of age (het ZFP, $n=25$; het vehicle, $n=26$; wt vehicle, $n=25$)
946 following striatal injection at 5 months of age. One-way ANOVA with Tukey's multiple

947 comparison test; ARG = autoradiography. Data are shown as mean \pm s.d., all points shown;
948 * P <0.05, ** P <0.01, *** P <0.001, **** P <0.0001.

949

950



952 **Fig. 5. Modulation of [¹¹C]CHDI-180R binding by broadly distributed mHTT lowering in**
953 **LacQ140^I(*) het mice. (A)** Schematic overview of the LacQ140^I(*) allele. The transcriptional
954 repressor, LacIR, binds to the Lac Operator, LacO, precluding expression of the Q140 allele (top).
955 Administration of isopropyl β-d-1-thiogalactopyranoside, IPTG, allosterically inhibits LacIR,
956 allowing transcription of the Q140 allele. **(B)** Timeline overview and endpoints in LacQ140^I(*) wt
957 and het mice. **(C)** Mean [¹¹C]CHDI-180R V_T (IDIF) parametric images of LacQ140^I(*) wt and het
958 mice at 13 months of age. PET images are co-registered to the MRI template for anatomical
959 reference. Coronal and axial planes are shown. **(D)** Regional [¹¹C]CHDI-180R V_T (IDIF)
960 quantification in LacQ140^I(*) wt and het at 13 months (het no supp, $n=14$; het 8-13m, $n=14$; het
961 2-13m, $n=13$; wt no supp, $n=11$) of age. One-way ANOVA with Tukey's multiple comparison
962 test. **(E,H)** Representative autoradiograms showing total binding of [³H]CHDI-00485180 (mHTT
963 inclusions) **(E)** and immunostaining as demonstrated by mEM48 **(H)** in LacQ140^I(*) wt and het
964 mice. Scale bar, 10 μm. **(F,I)** Specific binding of [³H]CHDI-00485180 **(F)** and quantification of
965 inclusions for mEM48 **(I)** in LacQ140^I(*) wt and het mice at 13 months of age (het no supp, $n=13$;
966 het 8-13m, $n=13$; het 2-13m, $n=13$; wt no supp, $n=12$). One-way ANOVA with Tukey's multiple
967 comparison test. **(G)** Correlation between striatal mHTT binding measured with microPET and
968 autoradiography in LacQ140^I(*) wt and het mice at 13 months of age. Two-tailed Pearson
969 correlation analysis; $R^2=0.779$; $P<0.0001$. **(J)** Correlation between striatal mHTT binding
970 measured with microPET and immunostaining in LacQ140^I(*) wt and het mice at 13 months of
971 age. Two-tailed Pearson correlation analysis; $R^2=0.794$; $P<0.0001$. ARG = autoradiography. Data
972 are shown as mean ± s.d., all points shown; * $P<0.05$, ** $P<0.01$, *** $P<0.001$, **** $P<0.0001$.

973

974

975

976